Supporting Information

Figure S1. Snapshots of melting droplets of LuC_2 and TbC_2.

Table S1. Summary of Le Bail fits and EDX analyses of $Tb_xU_{1-x}C_2$.

Figure S1.1. Lattice parameters *a* and *c* of $Tb_xU_{1-x}C_2$ in dependence of x.

Figure S1.2. Sections of the synchrotron powder diffraction patterns of $Tb_xU_{1-x}C_2$ in dependence of x.

Figure S1.3. Le Bail fits of $Tb_xU_{1-x}C_2$.

Table S2. Summary of Le Bail fits and EDX analyses of $Dy_xU_{1-x}C_2$.

Figure S2.1. Lattice parameters *a* and *c* of $Dy_xU_{1-x}C_2$ in dependence of x.

Figure S2.2. Sections of the synchrotron powder diffraction patterns of $Dy_xU_{1-x}C_2$ in dependence of x.

Figure S2.3. Le Bail fits of $Dy_xU_{1-x}C_2$.

Table S3. Summary of Le Bail fits and EDX analyses of $Ho_xU_{1-x}C_2$.

Figure S3.1. Lattice parameters *a* and *c* of $Ho_xU_{1-x}C_2$ in dependence of x.

Figure S3.2. Sections of the synchrotron powder diffraction patterns of $Ho_xU_{1-x}C_2$ in dependence of x.

Figure S3.3. Le Bail fits of $Ho_xU_{1-x}C_2$.

Table S4. Summary of Le Bail fits and EDX analyses of $Tm_xU_{1-x}C_2$.

Figure S4.1. Lattice parameters *a* and *c* of $Tm_xU_{1-x}C_2$ in dependence of x.

Figure S4.2. Sections of the synchrotron powder diffraction patterns of $Tm_xU_{1-x}C_2$ in dependence of x.

Figure S4.3. Le Bail fits of $Tm_xU_{1-x}C_2$.

Table S5. Summary of Le Bail fits on $Lu_xU_{1-x}C_2$.

Figure S5.1. Lattice parameters *a* and *c* of $Lu_xU_{1-x}C_2$ in dependence of x.

Figure S5.2. Sections of the synchrotron powder diffraction patterns of $Lu_xU_{1-x}C_2$ in dependence of x.

Figure S5.3. Le Bail fits of $Lu_xU_{1-x}C_2$.

Table S6. Summary of results of XANES spectra of $Tb_xU_{1-x}C_2$.

Figure S6.1. XANES spectra of $Tb_xU_{1-x}C_2$ at the Tb-L_{III} and U-L_{III} edge.

Figure S6.2. Graphical summary of the results of the XANES spectra of $Tb_xU_{1-x}C_2$ at the Tb-L_{III} and U-L_{III} edge.

Figure S6.3. Fits of the XANES spectra of $Tb_xU_{1-x}C_2$ at the Tb-L_{III} edge.

Figure S6.4. Fits of the XANES spectra of $Tb_xU_{1-x}C_2$ at the U-L_{III} edge.

Table S7. Summary of results of XANES spectra of $Dy_xU_{1-x}C_2$.

Figure S7.1. XANES spectra of $Dy_xU_{1-x}C_2$ at the Dy-L_{III} and U-L_{III} edge.

Figure S7.2. Graphical summary of the results of the XANES spectra of $Dy_xU_{1-x}C_2$ at the Dy-L_{III} and U-L_{III} edge.

Figure S7.3. Fits of the XANES spectra of $Dy_xU_{1-x}C_2$ at the Dy-L_{III} edge.

Figure S7.4. Fits of the XANES spectra of $Dy_xU_{1-x}C_2$ at the U-L_{III} edge.

Table S8. Summary of results of XANES spectra of $Ho_xU_{1-x}C_2$.

Figure S8.1. XANES spectra of $Ho_xU_{1-x}C_2$ at the Ho-L_{III} and U-L_{III} edge.

Figure S8.2. Graphical summary of the results of the XANES spectra of $Ho_xU_{1-x}C_2$ at the Ho-L_{III} and U-L_{III} edge.

Figure S8.3. Fits of the XANES spectra of $Ho_xU_{1-x}C_2$ at the Ho-L_{III} edge.

Figure S8.4. Fits of the XANES spectra of $Ho_xU_{1-x}C_2$ at the U-L_{III} edge.

Table S9. Summary of results of XANES spectra of $Tm_xU_{1-x}C_2$.

Figure S9.1. XANES spectra of $Tm_xU_{1-x}C_2$ at the Tm-L_{III} and U-L_{III} edge.

Figure S9.2. Graphical summary of the results of the XANES spectra of $Tm_xU_{1-x}C_2$ at the Tm-L_{III} and U-L_{III} edge.

Figure S9.3. Fits of the XANES spectra of $Tm_xU_{1-x}C_2$ at the Tm-L_{III} edge.

Figure S9.4. Fits of the XANES spectra of $Tm_xU_{1-x}C_2$ at the U-L_{III} edge.

Table S10. Summary of results of XANES spectra of $Lu_xU_{1-x}C_2$.

Figure S10.1. XANES spectra of $Lu_xU_{1-x}C_2$ at the Lu-L_{III} and U-L_{III} edge.

Figure S10.2. Graphical summary of the results of the XANES spectra of $Lu_xU_{1-x}C_2$ at the Lu-L_{III} and U-L_{III} edge.

Figure S10.3. Fits of the XANES spectra of $Lu_xU_{1-x}C_2$ at the Lu-L_{III} edge.

Figure S10.4. Fits of the XANES spectra of $Lu_xU_{1-x}C_2$ at the U-L_{III} edge.

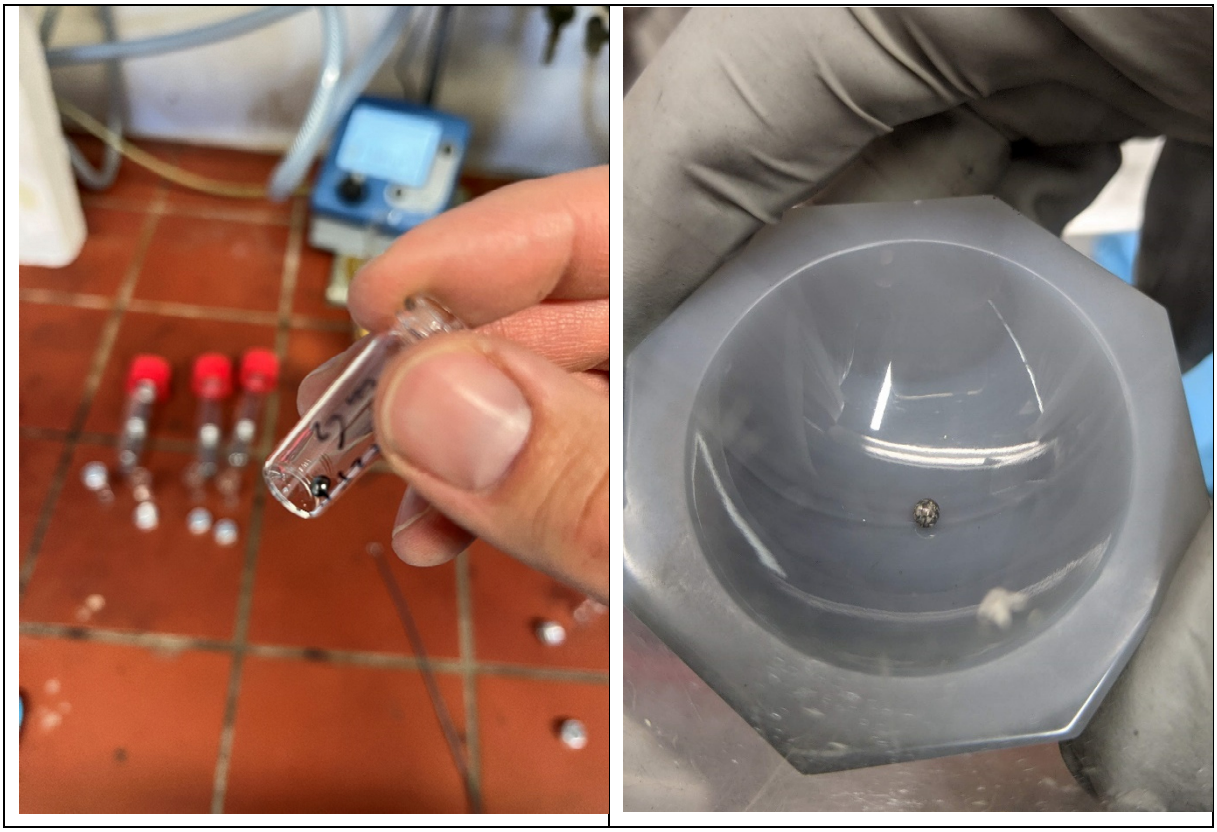

Figure S1. Snapshots of typical melting droplets of LuC_2 (left) and TbC_2 (right).

Table S1. Summary of Le Bail fits and EDX analyses of $Tb_xU_{1-x}C_2$.

x_{nom} / %	x(EDX) / %	*a* / Å	*c* / Å	*V* / Å^3	R_p	wR_p
0	0	3.52052(7)	5.9709(2)	74.004(4)	0.0623	0.0908
10	9.1(3)	3.53110(6)	5.9877(2)	74.659(3)	0.0636	0.0906
30	30.7(4)	3.57187(11)	6.0470(3)	77.150(6)	0.0642	0.0874
50	52.1(1)	3.62402(6)	6.12496(12)	80.442(3)	0.0406	0.0532
70	67.2(4)	3.64713(9)	6.1402(2)	81.674(5)	0.0473	0.0665
90	91.6(5)	3.68172(3)	6.19640(8)	83.993(2)	0.0223	0.0318
100	100	3.68785(3)	6.19854(6)	84.3017(14)	0.0176	0.0245

Red: estimated errors.

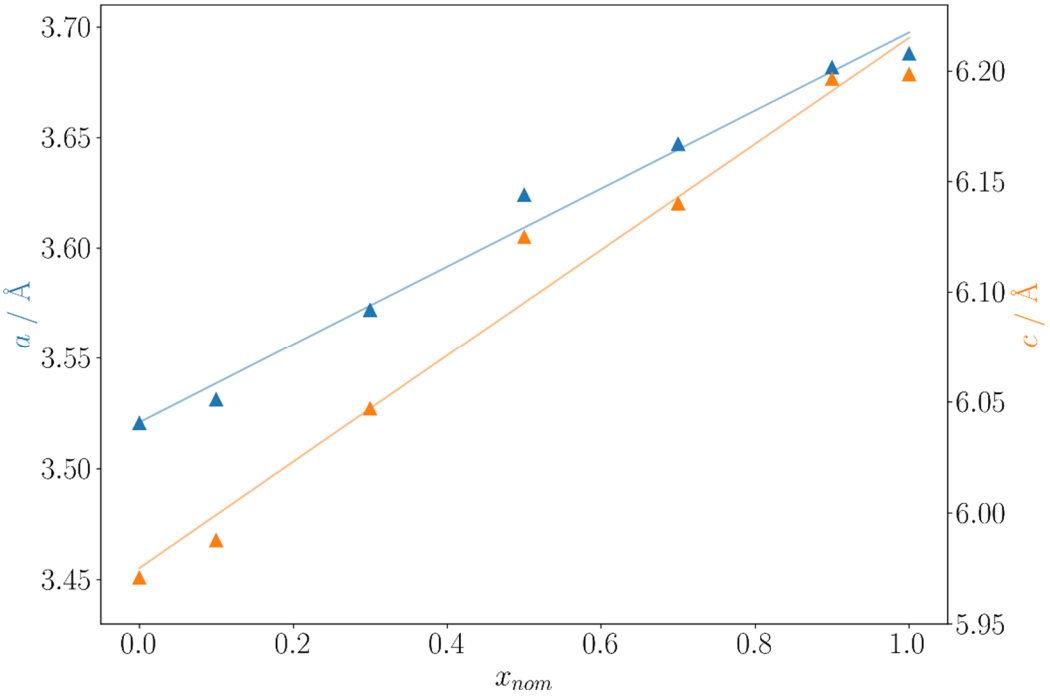

Figure S1.1. Lattice parameters *a* and *c* of $Tb_xU_{1-x}C_2$ in dependence of x_{nom}. The standard deviations as obtained from Le Bail fits (Table S1) are smaller than the symbols of the plot.

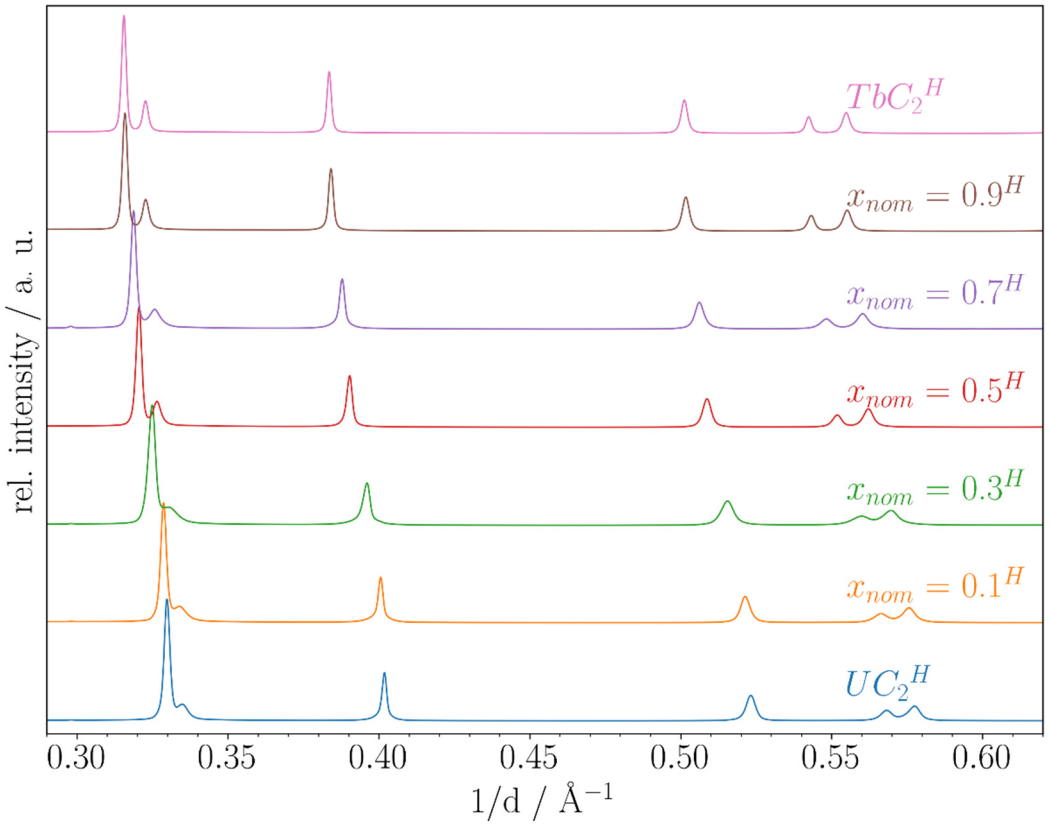

Figure S1.2. Sections of the synchrotron powder diffraction patterns of $Tb_xU_{1-x}C_2$ in dependence of x_{nom}; H: λ = 0.20735 Å.

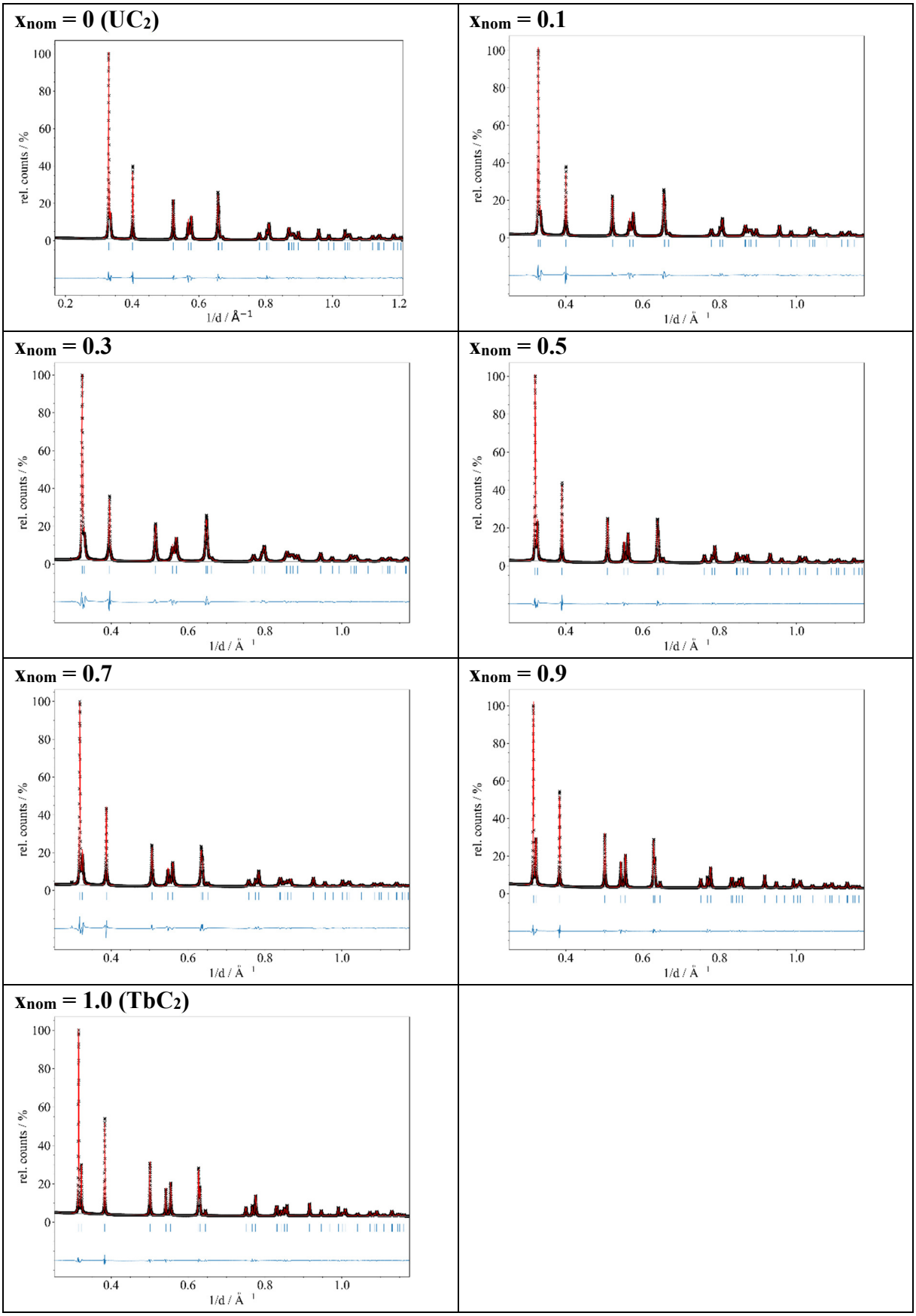

Figure S1.3. Le Bail fits of $Tb_xU_{1-x}C_2$.

Table S2. Summary of Le Bail fits and EDX analyses of $Dy_xU_{1-x}C_2$.

x_{nom} / %	x(EDX) / %	*a* / Å	*c* / Å	*V* / Å^3	R_p	wR_p
0	0	3.52052(7)	5.9709(2)	74.004(4)	0.0623	0.0908
10	6.1(4)	3.52426(5)	5.97777(12)	74.247(3)	0.0548	0.0812
30	21(2)	3.55001(5)	6.01574(13)	75.814(3)	0.0560	0.0803
50	48.8(15)	3.59061(9)	6.0745(2)	78.315(5)	0.0199	0.0283
70	60(3)	3.6193(1)	6.1073(2)	80.003(5)	0.0419	0.0597
90	92.0(7)	3.65875(7)	6.1552(2)	82.397(4)	0.0217	0.0335
100	100	3.66855(5)	6.16602(12)	82.984(3)	0.0243	0.0376

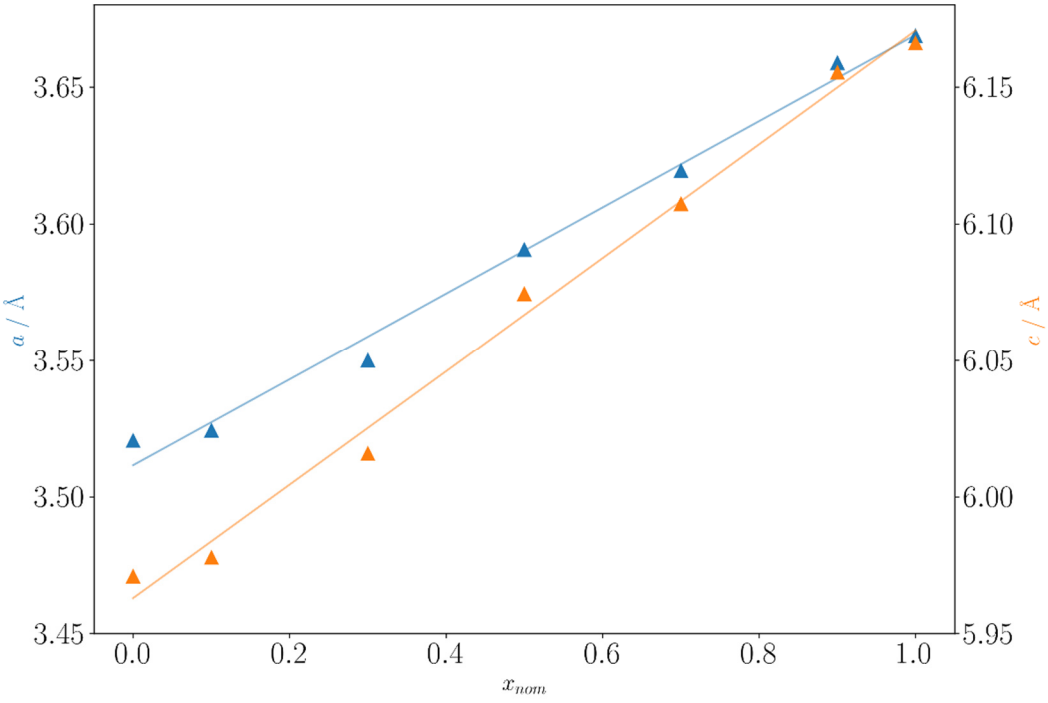

Figure S2.1. Lattice parameters *a* and *c* of $Dy_xU_{1-x}C_2$ in dependence of x_{nom}. The standard deviations as obtained from Le Bail fits (Table S2) are smaller than the symbols of the plot.

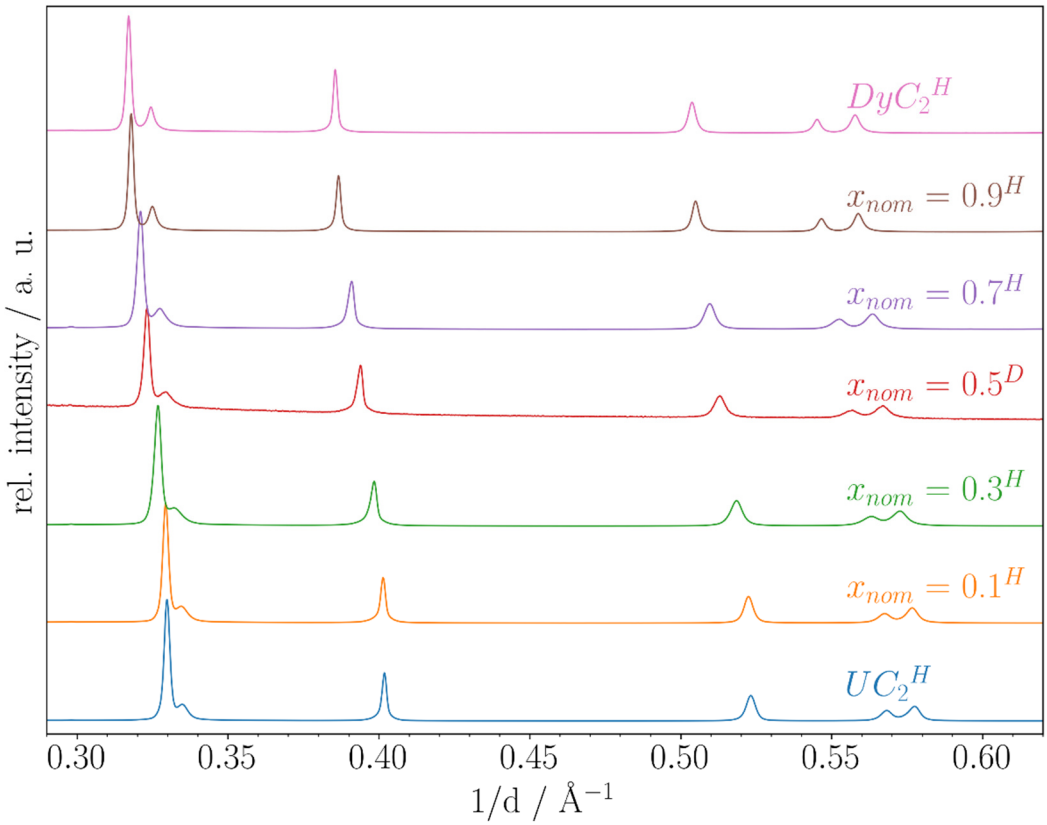

Figure S2.2. Sections of the synchrotron powder diffraction patterns of $Dy_xU_{1-x}C_2$ in dependence of x_{nom}; H: λ = 0.20735 Å, D: λ = 0.4959 Å.

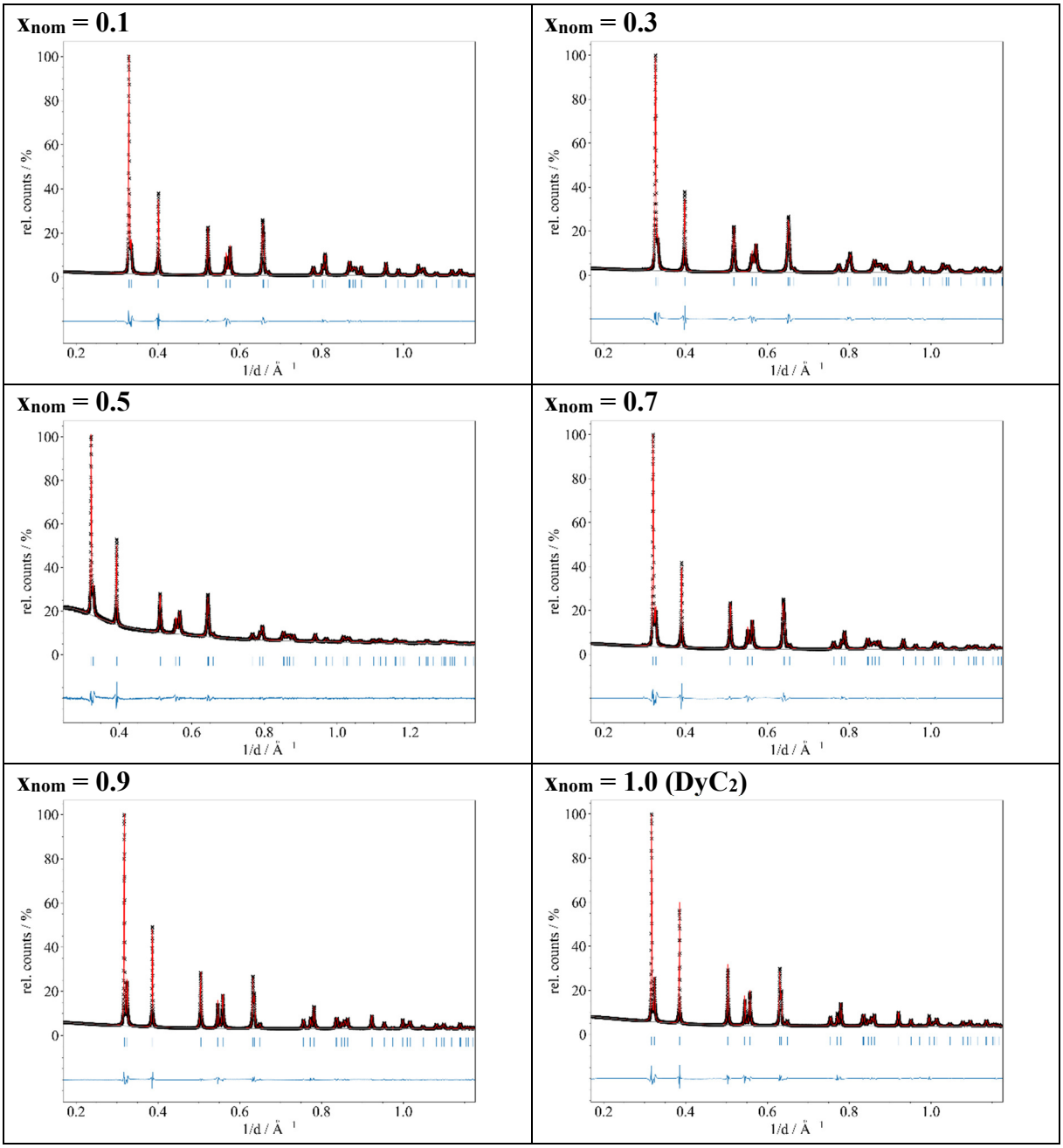

Figure S2.3. Le Bail fits of $Dy_xU_{1-x}C_2$; x = 0 (UC_2) see Figure S1.3.

Table S3. Summary of Le Bail fits and EDX analyses of $Ho_xU_{1-x}C_2$.

x_{nom} / %	x(EDX) / %	*a* / Å	*c* / Å	*V* / Å^3	R_p	wR_p
0	0	3.52052(7)	5.9709(2)	74.004(4)	0.0623	0.0908
10	4.3(3)	3.52025(5)	5.97541(11)	74.048(2)	0.0568	0.0829
30	24.3(3)	3.54817(5)	6.0104(2)	75.668(3)	0.0455	0.0663
50	45.5(4)	3.57982(7)	6.0587(2)	77.643(4)	0.0357	0.0499
70	66.4(3)	3.61598(8)	6.1066(2)	79.846(4)	0.0347	0.0528
90	90.7(2)	3.63608(4)	6.13339(9)	81.090(2)	0.0361	0.0483
100	100	3.64411(4)	6.1405(1)	81.543(2)	0.0219	0.0319

Red: estimated errors.

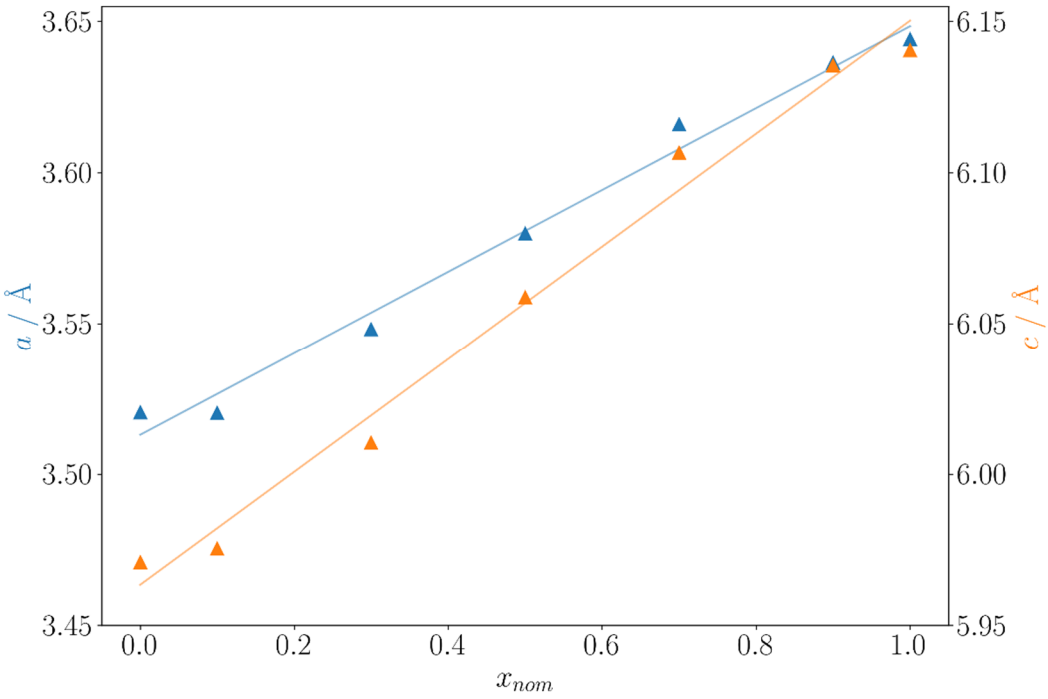

Figure S3.1. Lattice parameters *a* and *c* of $Ho_xU_{1-x}C_2$ in dependence of x_{nom}. The standard deviations as obtained from Le Bail fits (Table S3) are smaller than the symbols of the plot.

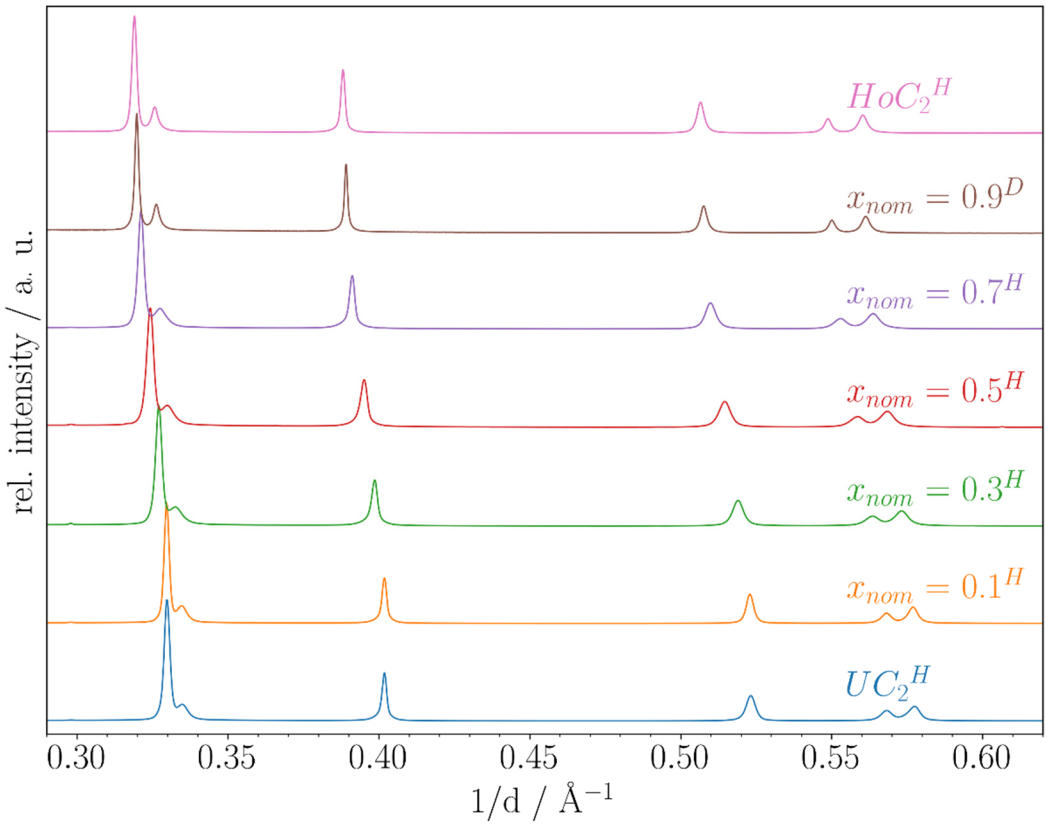

Figure S3.2. Sections of the synchrotron powder diffraction patterns of $Ho_xU_{1-x}C_2$ in dependence of x_{nom}; H: λ = 0.20735 Å; D: λ = 0.4959 Å.

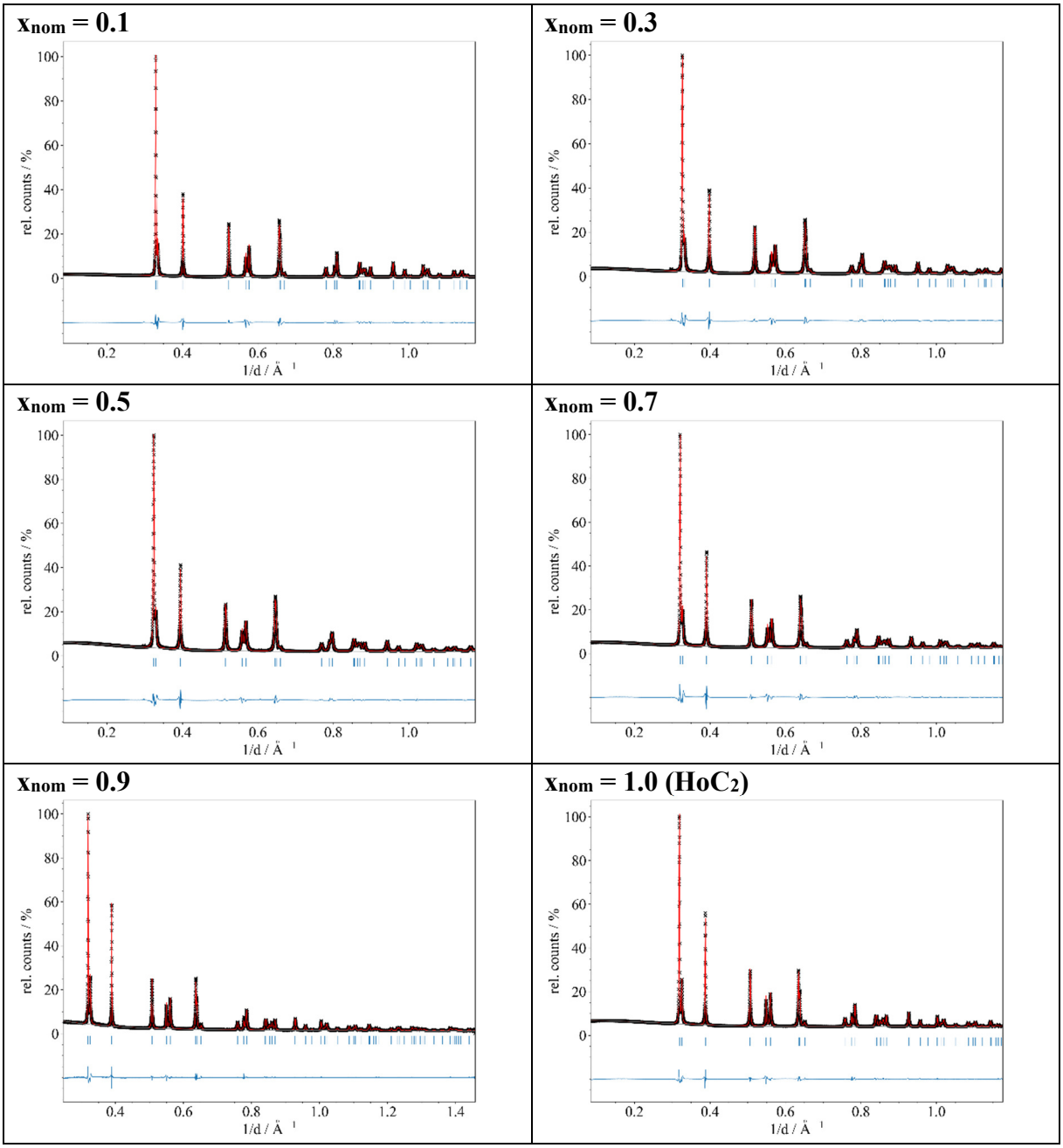

Figure S3.3. Le Bail fits of $Ho_xU_{1-x}C_2$; x = 0 (UC_2) see Figure S1.3.

Table S4. Summary of Le Bail fits and EDX analyses of $Tm_xU_{1-x}C_2$.

x_{nom} / %	x(EDX) / %	*a* / Å	*c* / Å	*V* / Å^3	R_p	wR_p
0	0	3.52052(7)	5.9709(2)	74.004(4)	0.0623	0.0908
10	4.6(8)	3.51811(5)	5.97120(11)	73.906(2)	0.0572	0.0815
30	24.3(12)	3.53618(7)	5.9911(2)	74.916(4)	0.0429	0.0620
50	38(4)	3.55464(7)	6.0056(2)	75.883(3)	0.0289	0.0422
70	69.8(13)	3.57804(6)	6.0311(2)	77.213(3)	0.0243	0.0337
90	90.6(2)	3.59694(9)	6.0451(2)	78.212(5)	0.0315	0.0484
100	100	3.6043(1)	6.0543(2)	78.653(5)	0.0600	0.0828

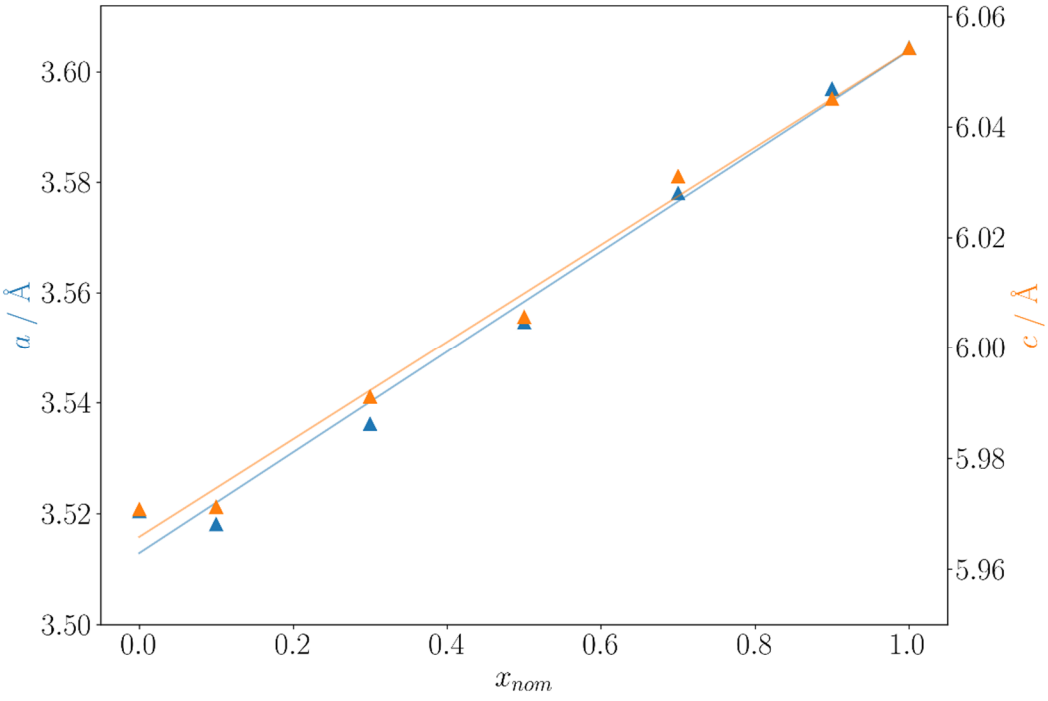

Figure S4.1. Lattice parameters *a* and *c* of $Tm_xU_{1-x}C_2$ in dependence of x_{nom}. The standard deviations as obtained from Le Bail fits (Table S4) are smaller than the symbols of the plot.

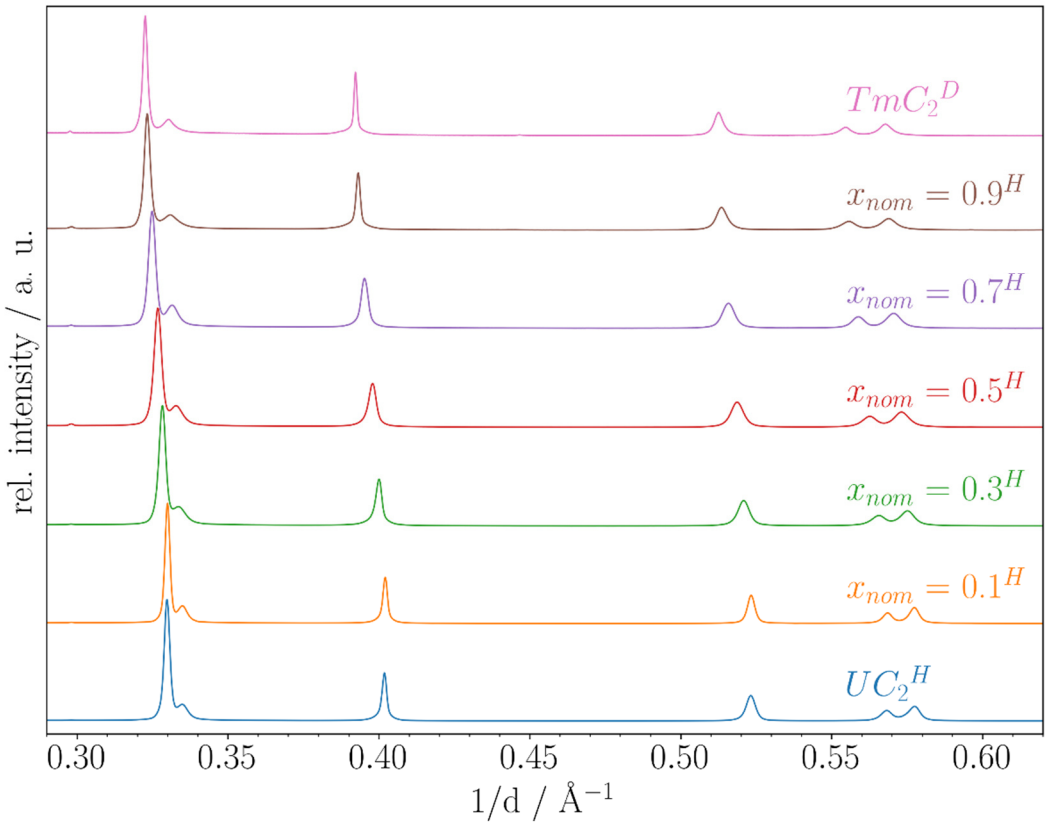

Figure S4.2. Sections of the synchrotron powder diffraction patterns of $Tm_xU_{1-x}C_2$ in dependence of x_{nom}; H: λ = 0.20735 Å; D: λ = 0.4959 Å.

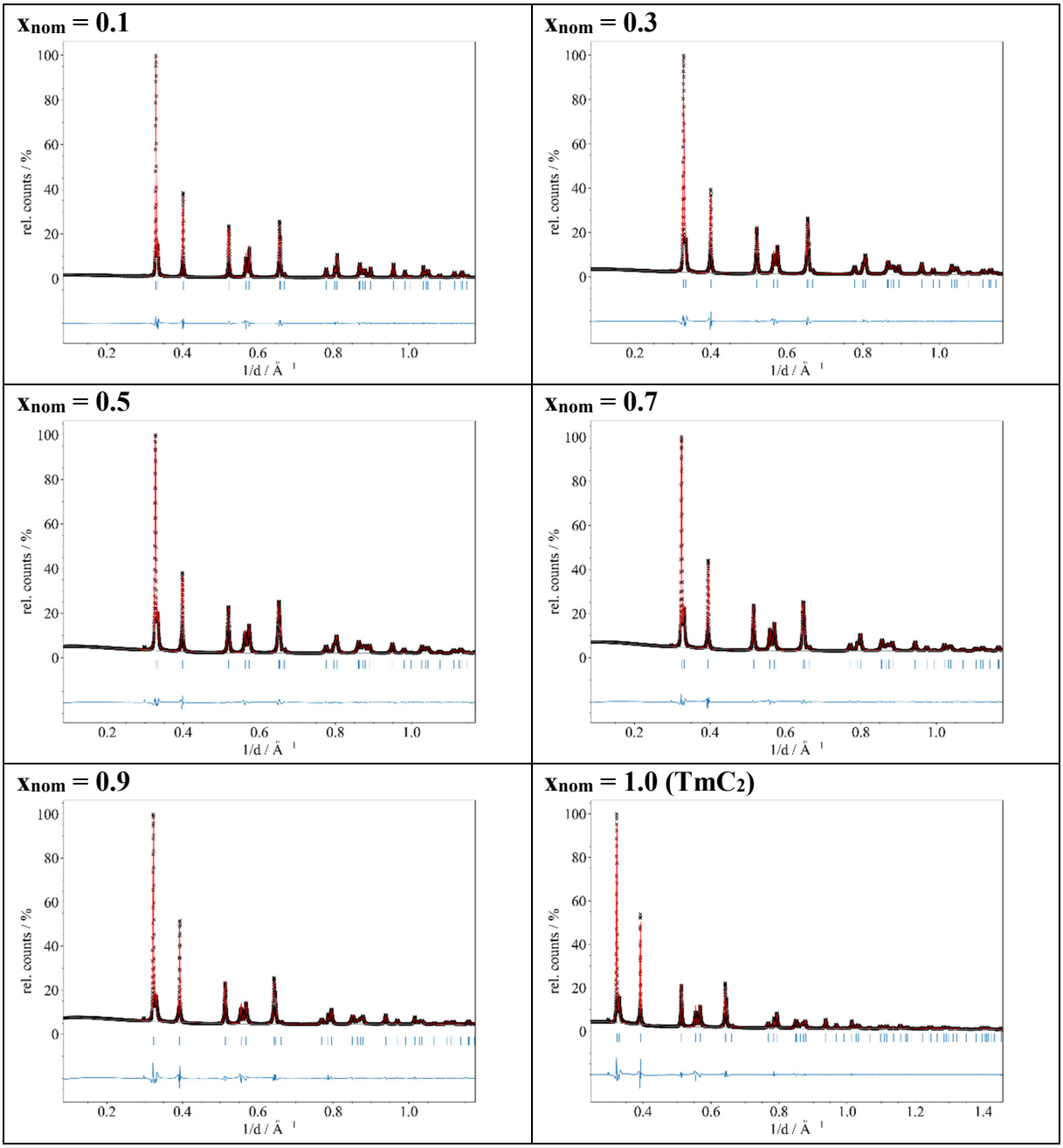

Figure S4.3. Le Bail fits of $Tm_xU_{1-x}C_2$; x = 0 (UC_2) see Figure S1.3.

Table S5. Summary of Le Bail fits of $Lu_xU_{1-x}C_2$.

x_{nom} / %	a / Å	c / Å	V / Å^3	R_p	wR_p
0	3.52052(7)	5.9709(2)	74.004(4)	0.0623	0.0908
12.5	3.52260(6)	5.9771(2)	74.168(3)	0.0157	0.0209
25	3.53470(9)	5.99199(12)	74.865(4)	0.0233	0.0318
37.5	3.53921(7)	5.9878(2)	75.003(4)	0.0178	0.0228
50	3.54563(7)	5.9923(2)	75.333(4)	0.0232	0.0293
62.5	3.55392(7)	5.9931(2)	75.695(4)	0.0317	0.0252
75	3.55617(5)	5.9632(2)	75.412(3)	0.0446	0.0352
87.5	3.55993(11)	5.9872(3)	75.877(6)	0.0516	0.0365
100*				0.0411	0.0285

* Lu_4C_7 was obtained ($P2_1/c$) with a = 3.62973(8) Å, b = 13.4827(3) Å, c = 6.3590(2) Å, β = 103.533(1)°, V = 302.56(1) Å^3

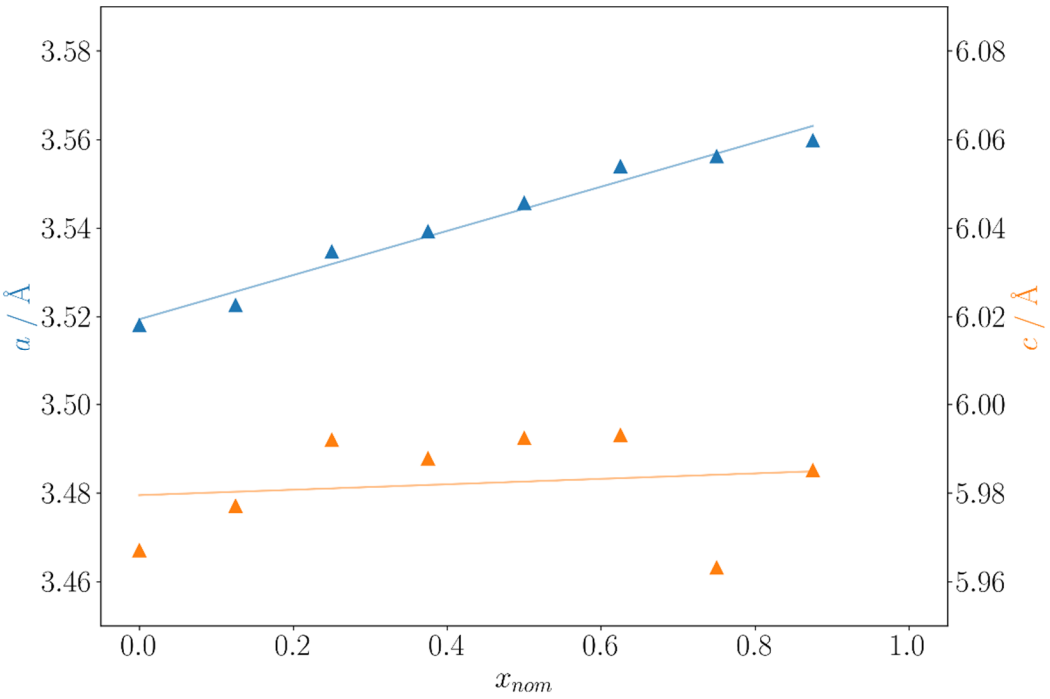

Figure S5.1. Lattice parameters a and c of $Lu_xU_{1-x}C_2$ in dependence of nominal x. The standard deviations as obtained from Le Bail fits (Table S5) are smaller than the symbols of the plot.

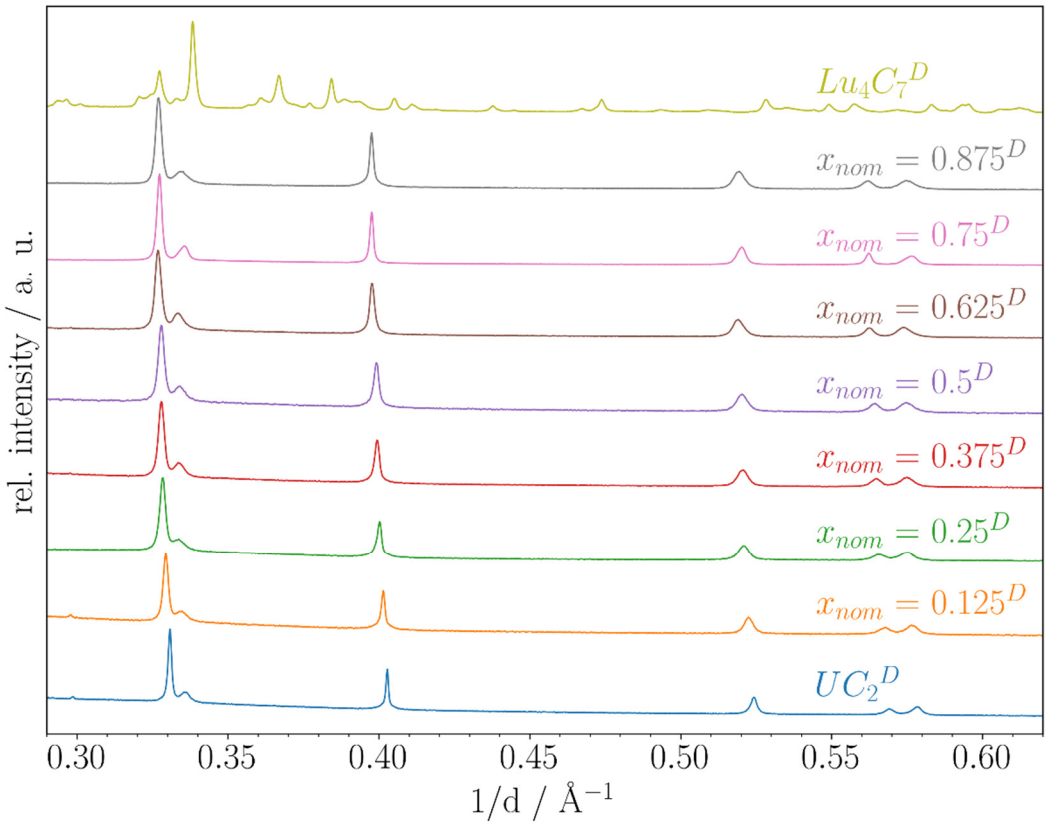

Figure S5.2. Sections of the synchrotron powder diffraction patterns of $Lu_xU_{1-x}C_2$ in dependence of x_{nom}; D: $\lambda = 0.4959$ Å.

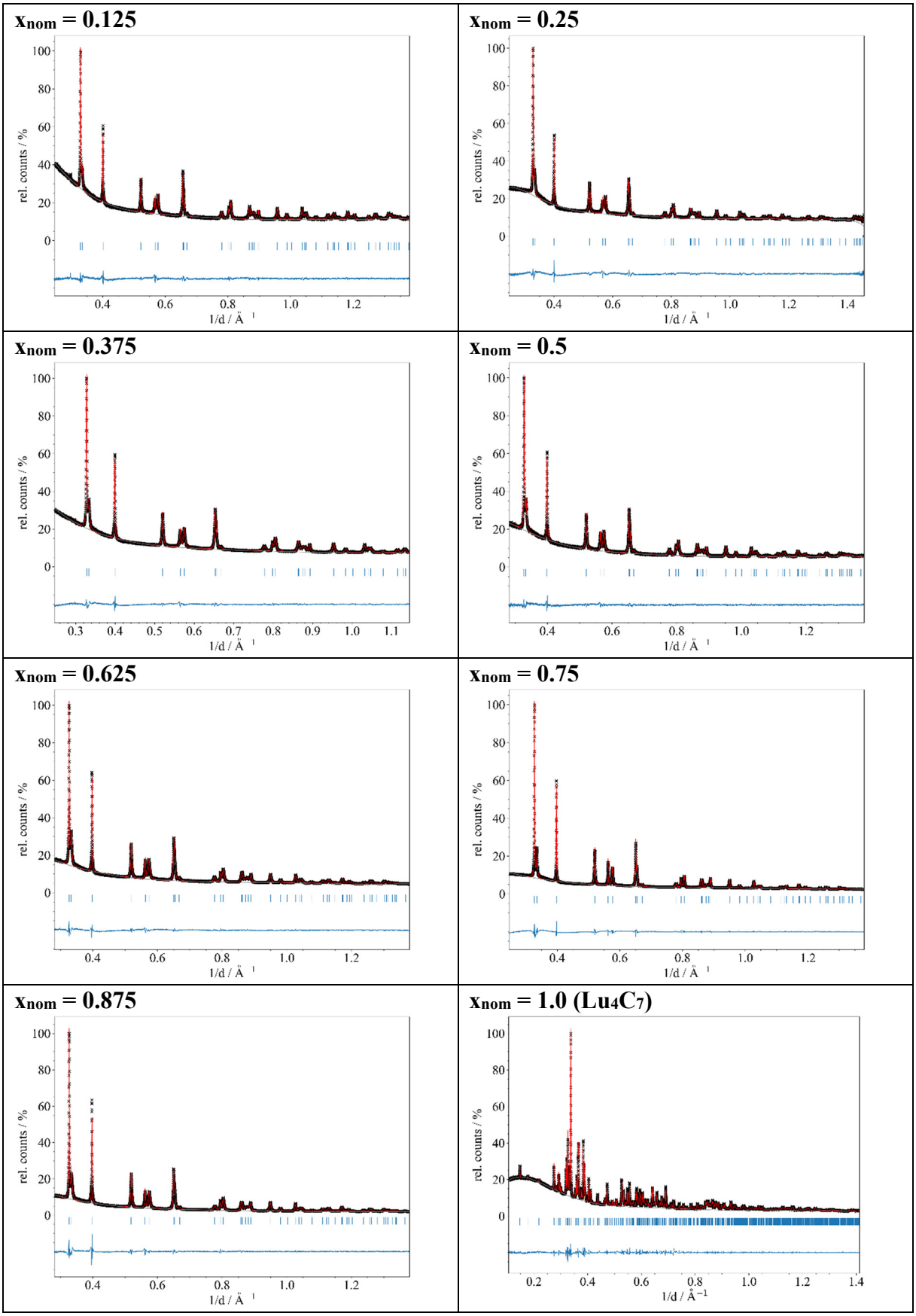

Figure S5.3. Le Bail fits of $Lu_xU_{1-x}C_2$; x = 0 (UC_2) see Figure S1.3.

Table S6. Summary of results of XANES spectra of $Tb_xU_{1-x}C_2$.

x_{nom} / %	x(EDX) / %	A_{WL} / a.u.		E_{WL} / eV		E_0 / eV	
		Tb-L_{III}	U-L_{III}	Tb-L_{III}	U-L_{III}	Tb-L_{III}	U-L_{III}
0	0	-	5.56	-	17175.65	-	17167.2
10	9.1(3)	-	4.36	-	17175.54	-	17166.2
30	30.7(4)	11.34	5.91	7519.79	17175.55	7516.08	17168.1
50	52.1(1)	8.30	6.02	7519.65	17175.30	7515.45	17167.7
70	67.2(4)	5.94	6.70	7519.54	17175.08	7514.55	17168.6
90	91.6(5)	3.75	7.12	7519.91	17174.68	7514.17	17168.7
100	100	4.15	-	7519.87	-	7514.47	-

Red: estimated errors.

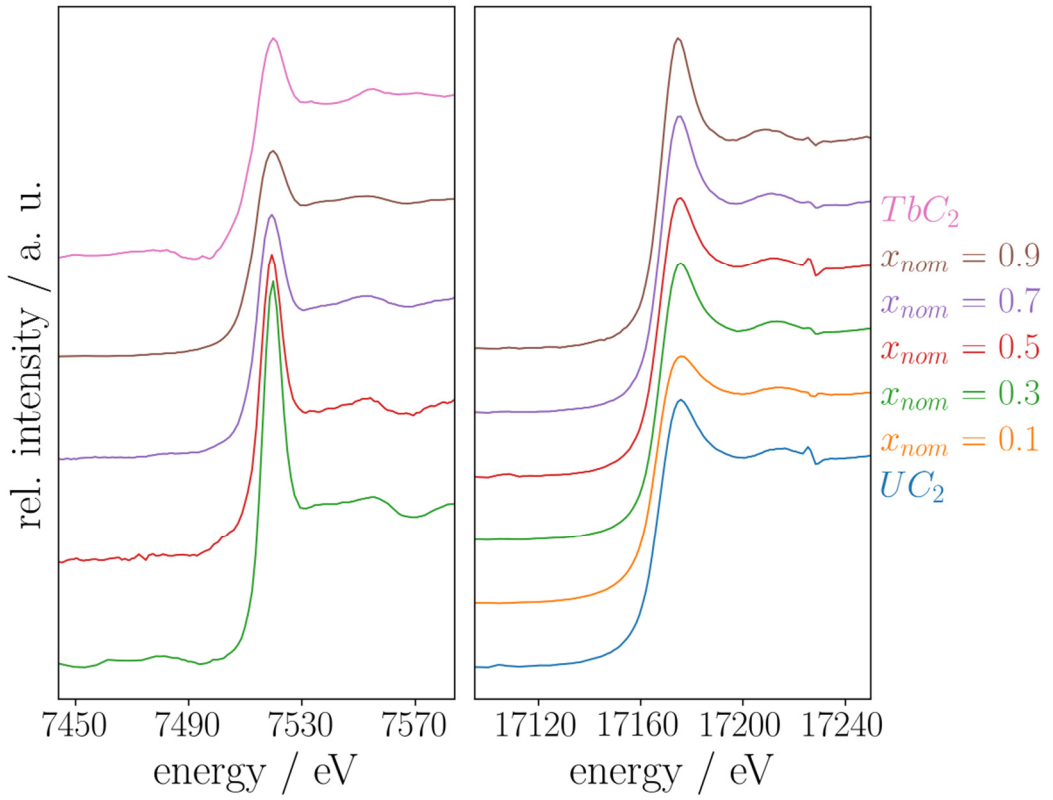

Figure S6.1. XANES spectra of $Tb_xU_{1-x}C_2$ at the Tb-L_{III} (left) and U-L_{III} edge (right).

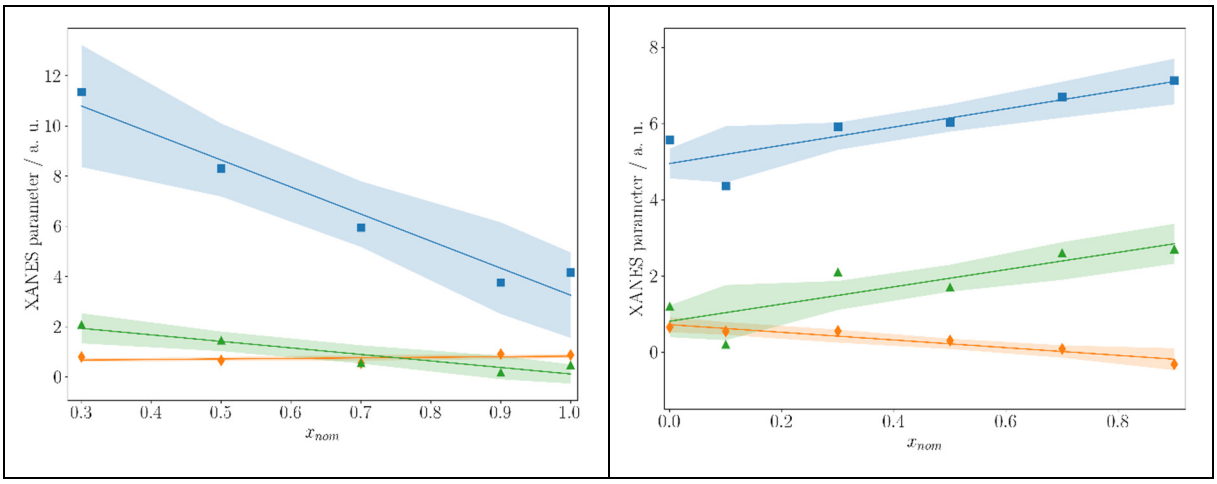

Figure S6.2. Graphical summary of the results of the XANES spectra of $Tb_xU_{1-x}C_2$ at the Tb-L_{III} (left) and U-L_{III} edge (right); blue: area of white line (A_{WL}), green: energy of white line (E_{WL}), orange: energy of absorption edge (E_0). The shaded areas correspond to confidence intervals of 68 %.

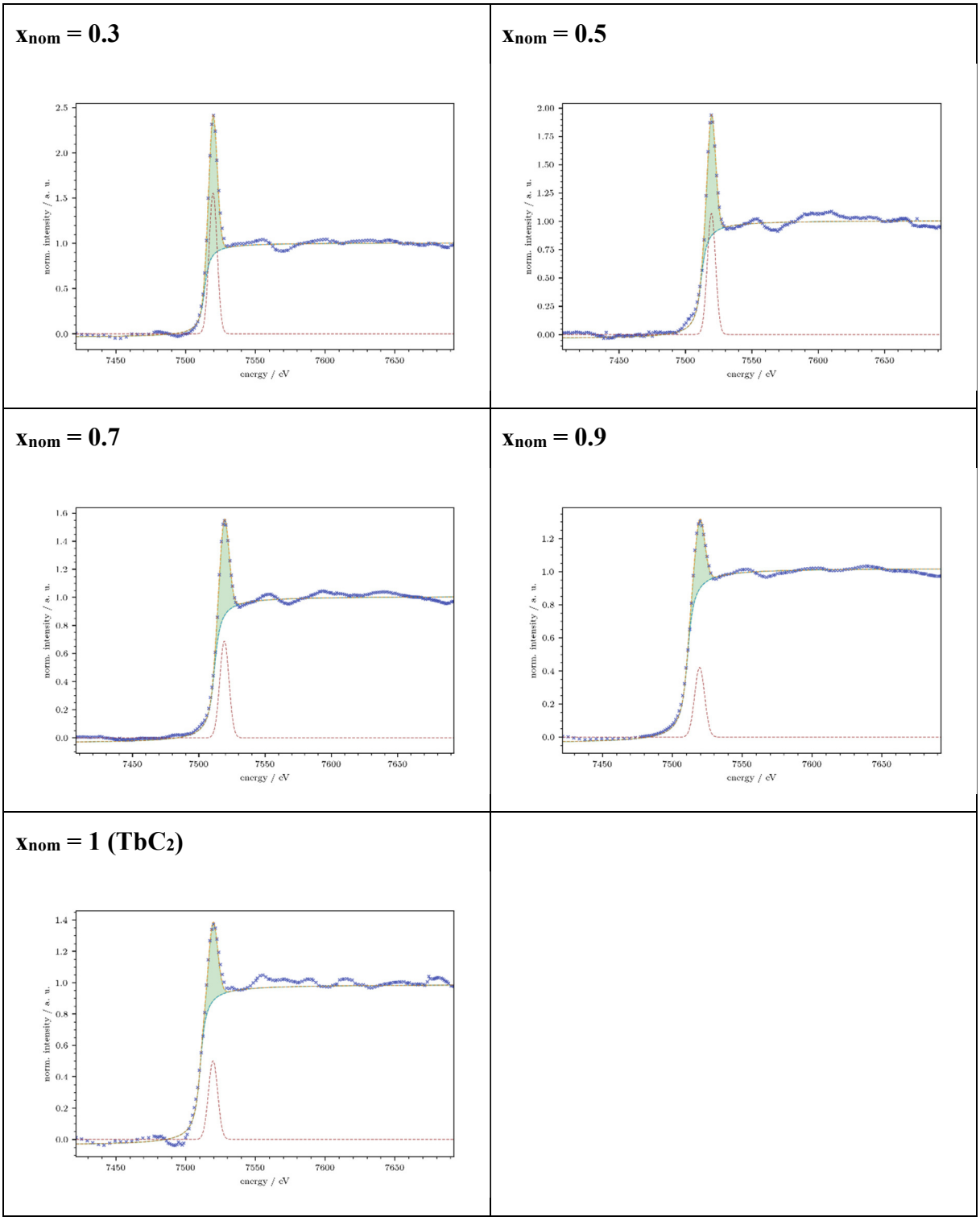

Figure S6.3. Fits of the XANES spectra of $Tb_xU_{1-x}C_2$ at the Tb-L_{III} edge.

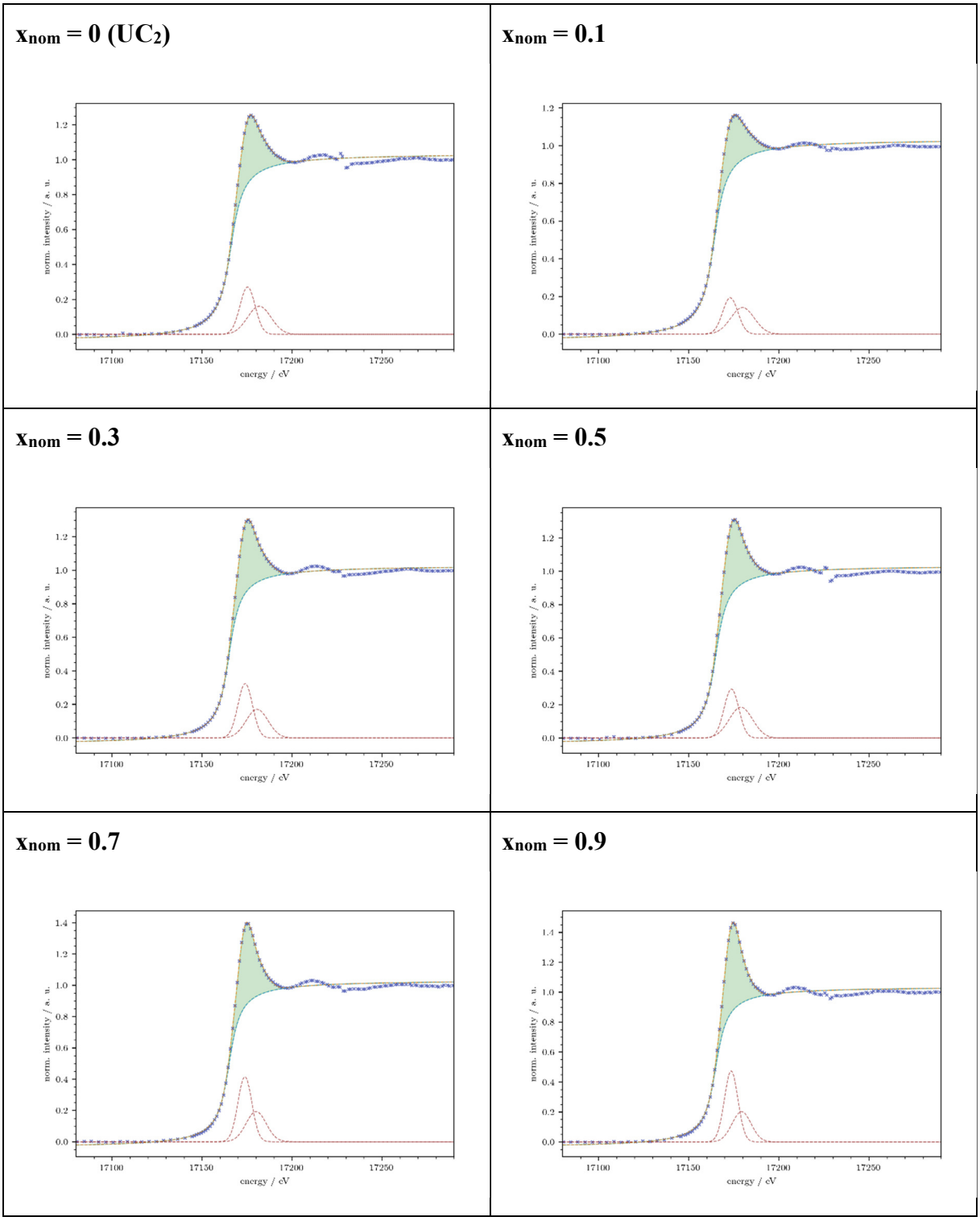

Figure S6.4. Fits of the XANES spectra of $Tb_xU_{1-x}C_2$ at the U-L_{III} edge.

Table S7. Summary of results of XANES spectra of $Dy_xU_{1-x}C_2$.

x_{nom} / %	x(EDX) / %	A_{WL} / a.u.		E_{WL} / eV		E_0 / eV	
		Dy-L_{III}	U-L_{III}	Dy-L_{III}	U-L_{III}	Dy-L_{III}	U-L_{III}
0	0	-	5.56	-	17175.65	-	17167.2
10	6.1(4)	5.39	5.24	7796.33	17175.72	7793.09	17167.2
30	21(2)	14.86	5.87	7796.31	17175.64	7792.52	17167.9
50	48.8(15)	9.04	9.88	7796.50	17177.45	7792.52	17171.9
70	60(3)	4.41	7.77	7796.48	17176.32	7790.63	17170.8
90	92.0(7)	4.44	6.89	7796.23	17174.72	7790.33	17168.4
100	100	6.19	-	7796.23	-	7791.24	-

Red: estimated errors.

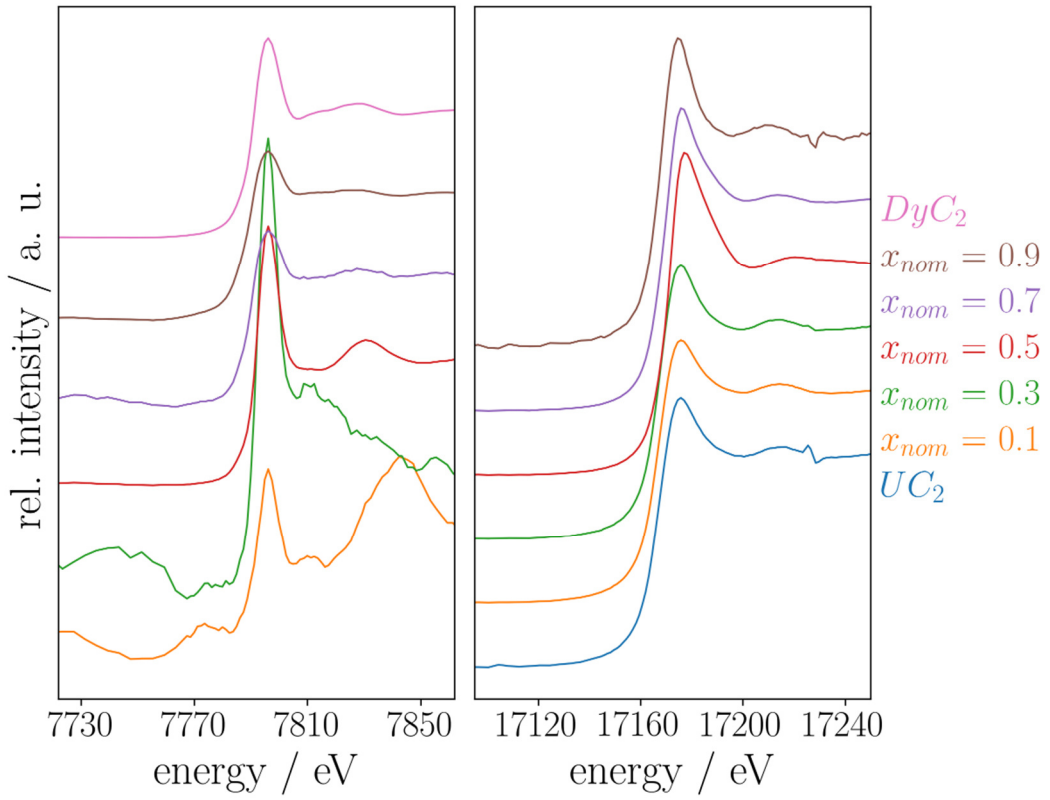

Figure S7.1. XANES spectra of $Dy_xU_{1-x}C_2$ at the Dy-L_{III} (left) and U-L_{III} edge (right).

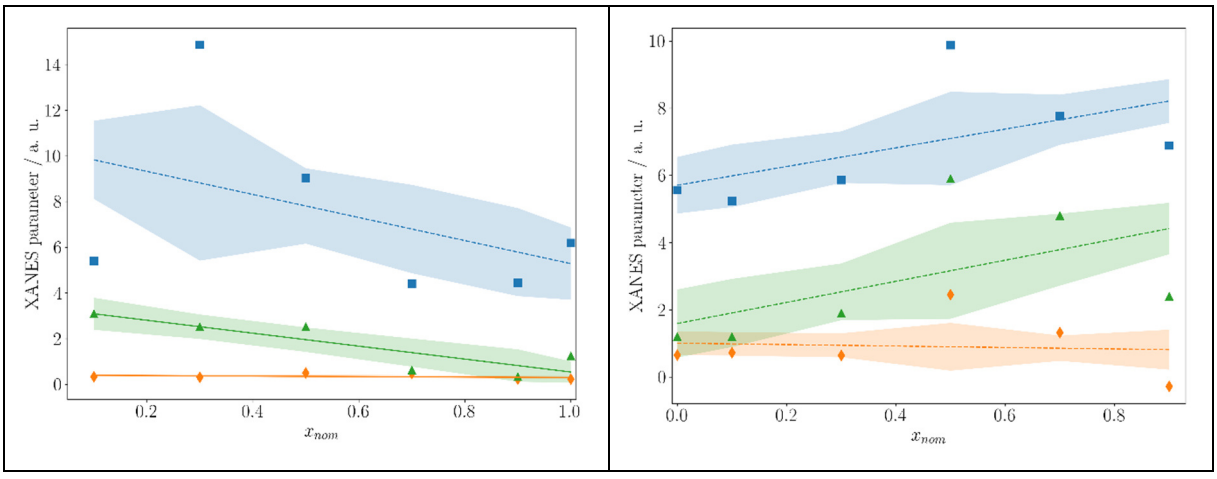

Figure S7.2. Graphical summary of the results of the XANES spectra of $Dy_xU_{1-x}C_2$ at the Dy-L_{III} (left) and U-L_{III} edge (right); blue: area of white line (A_{WL}), green: energy of white line (E_{WL}), orange: energy of absorption edge (E_0). The shaded areas correspond to confidence intervals of 68 %.

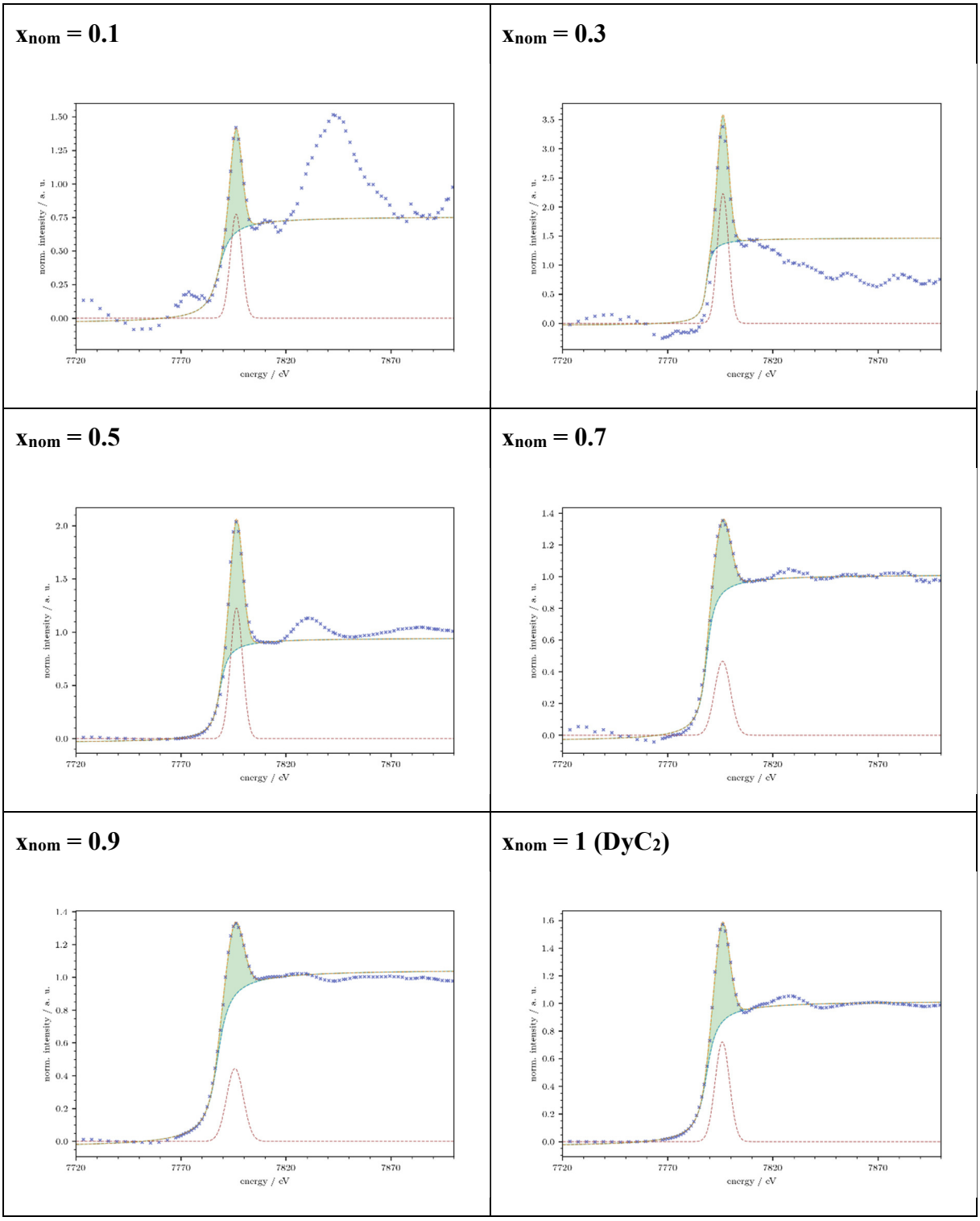

Figure S7.3. Fits of the XANES spectra of $Dy_xU_{1-x}C_2$ at the Dy-L_{III} edge.

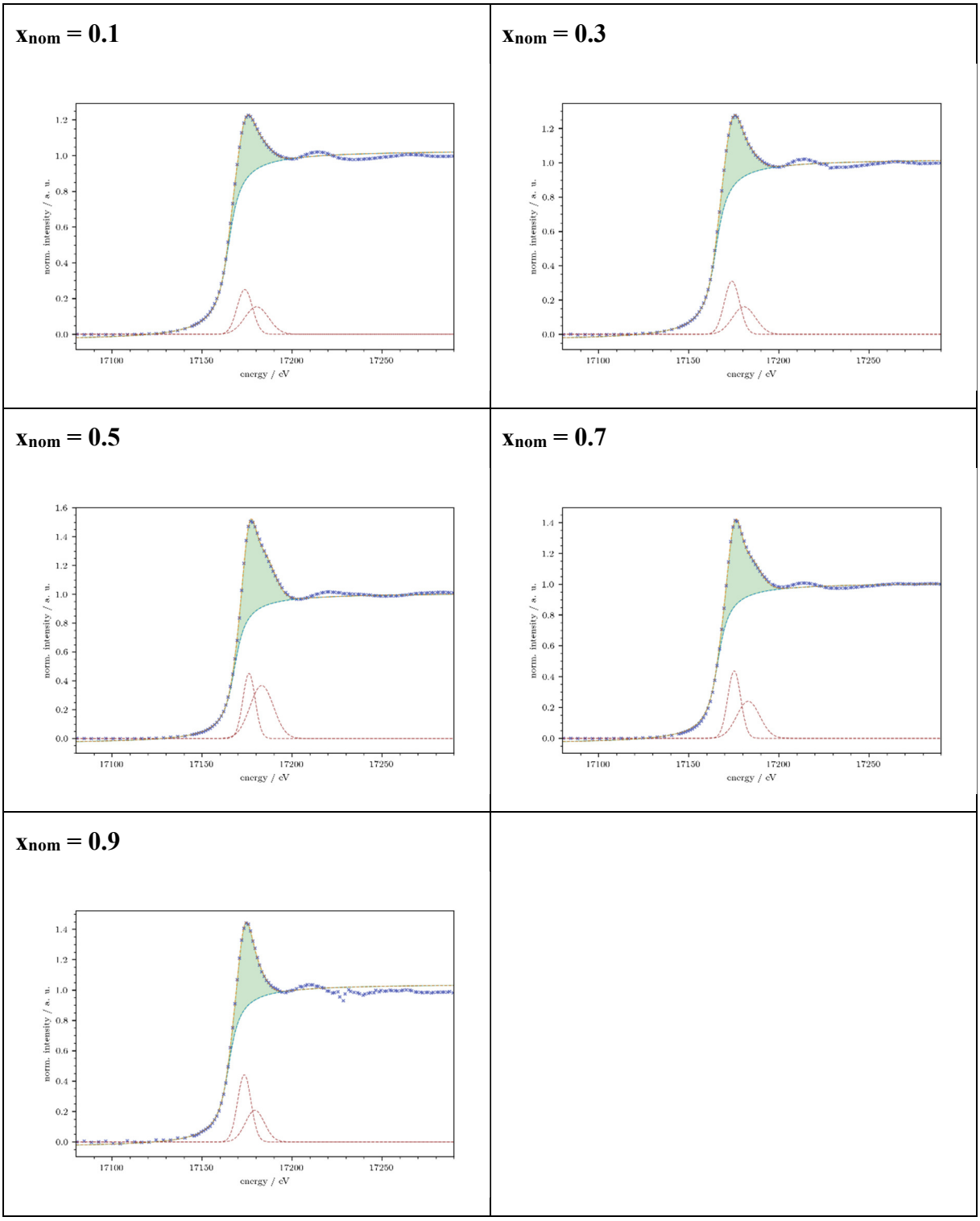

Figure S7.4. Fits of the XANES spectra of $Dy_xU_{1-x}C_2$ at the U-L_{III} edge; x = 0 (UC_2) see Figure S6.4.

Table S8. Summary of results of XANES spectra of $Ho_xU_{1-x}C_2$.

x_{nom} / %	x(EDX) / %	A_{WL} / a.u.		E_{WL} / eV		E_0 / eV	
		Ho-L_{III}	U-L_{III}	Ho-L_{III}	U-L_{III}	Ho-L_{III}	U-L_{III}
0	0	-	5.56	-	17175.65	-	17167.2
10	4.3(3)	(28.0)	5.73	8076.98	17175.76	8073.63	17167.8
30	24.3(3)	14.1	5.60	8077.06	17175.59	8073.25	17168.2
50	45.5(4)	8.5	6.20	8077.18	17175.36	8072.85	17168.2
70	66.4(3)	9.04	6.56	8078.25	17175.10	8072.98	17168.2
90	90.7(2)	6.46	7.81	8077.44	17174.83	8072.49	17168.7
100	100	2.57	-	8077.43	-	8070.87	-

Red: estimated errors.

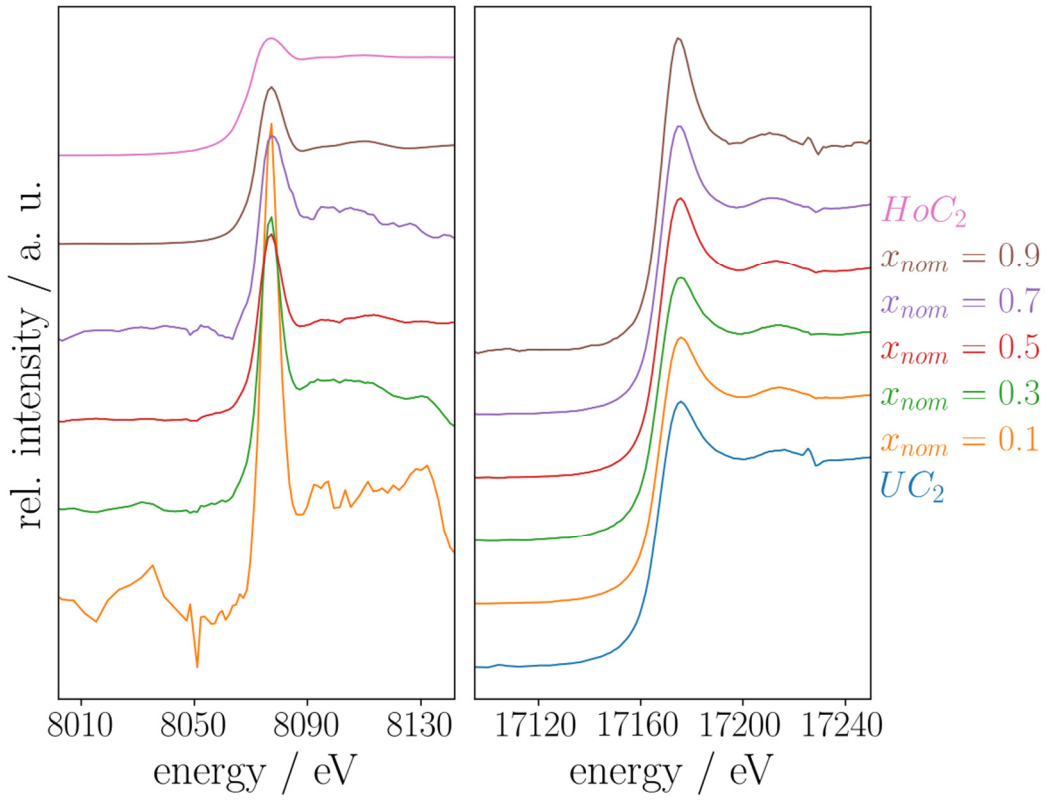

Figure S8.1. XANES spectra of $Ho_xU_{1-x}C_2$ at the Ho-L_{III} (left) and U-L_{III} edge (right).

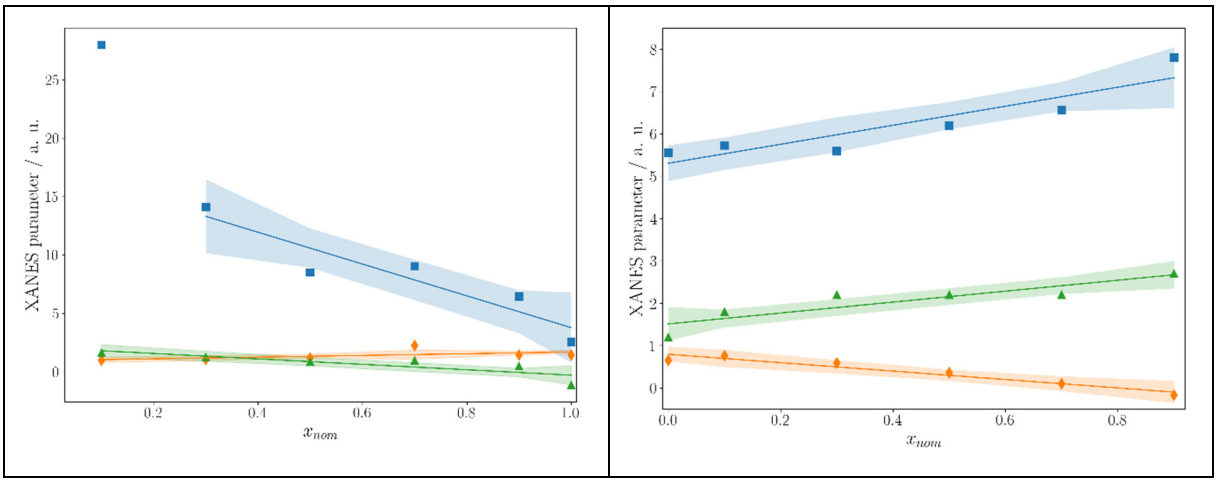

Figure S8.2. Graphical summary of the results of the XANES spectra of $Ho_xU_{1-x}C_2$ at the Ho-L_{III} (left) and U-L_{III} edge (right); blue: area of white line (A_{WL}), green: energy of white line (E_{WL}), orange: energy of absorption edge (E_0). The shaded areas correspond to confidence intervals of 68 %.

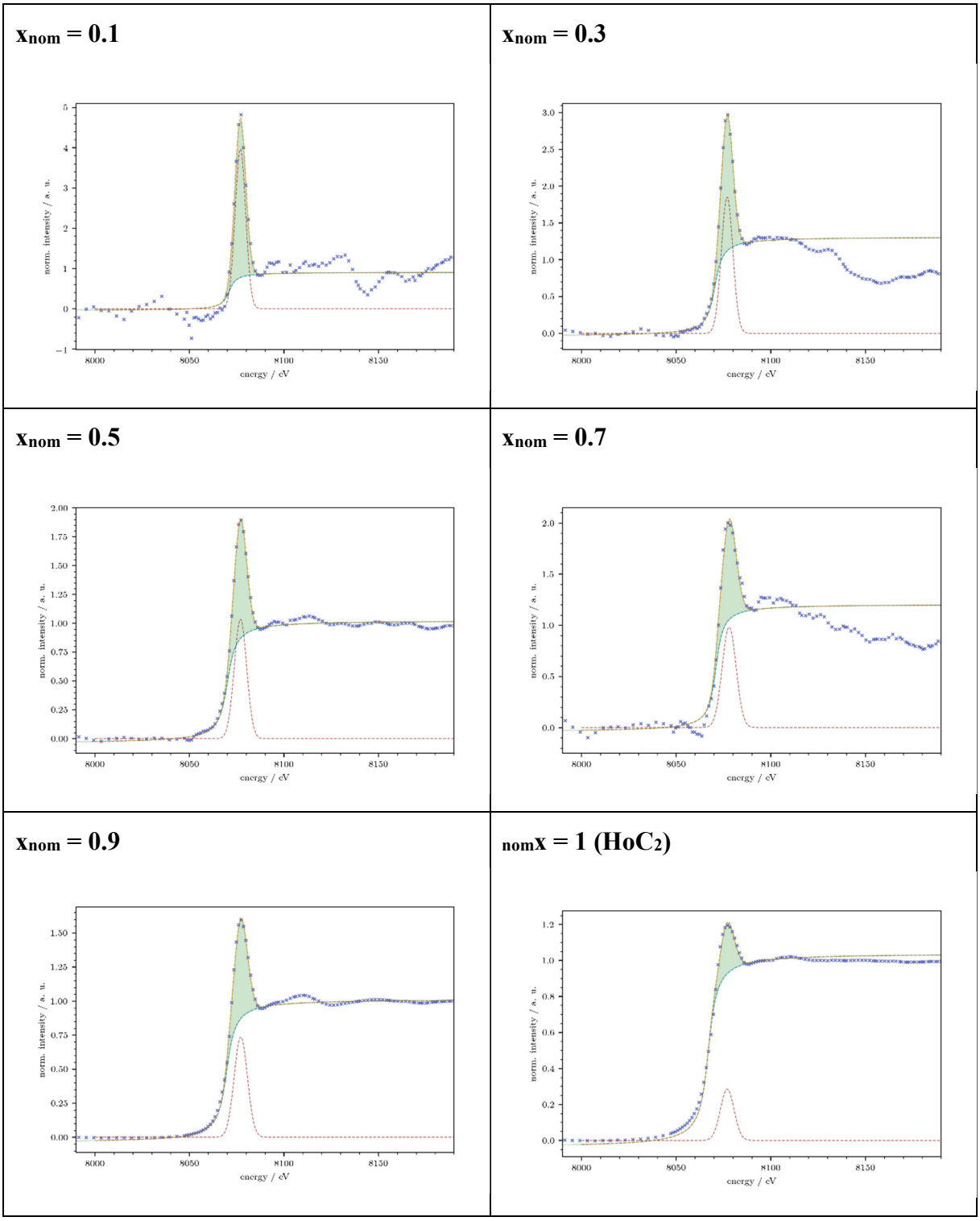

Figure S8.3. Fits of the XANES spectra of $Ho_xU_{1-x}C_2$ at the Ho-L_{III} edge.

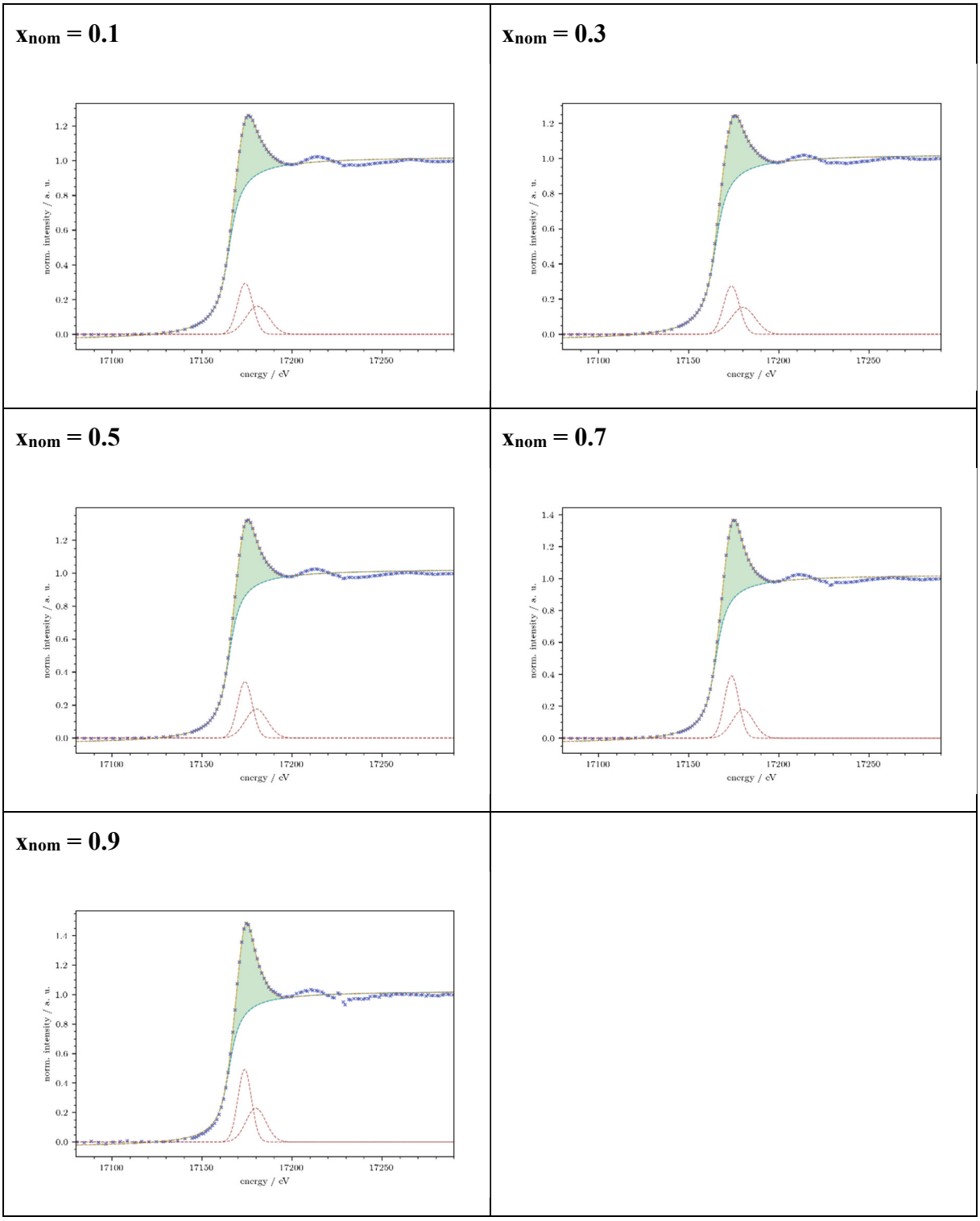

Figure S8.4. Fits of the XANES spectra of $Ho_xU_{1-x}C_2$ at the U-L_{III} edge; x = 0 (UC_2) see Figure S6.4.

Table S9. Summary of results of XANES spectra of $Tm_xU_{1-x}C_2$.

x_{nom} / %	x(EDX) / %	A_{WL} / a.u.		E_{WL} / eV		E_0 / eV	
		Tm-L_{III}	U-L_{III}	Tm-L_{III}	U-L_{III}	Tm-L_{III}	U-L_{III}
0	0	-	5.56	-	17175.65	-	17167.2
10	4.6(8)	8.61	5.39	8655.41	17175.77	8651.93	17167.2
30	24.3(12)	5.80	5.56	8655.08	17175.67	8650.72	17167.4
50	40.5(11)	11.23	6.77	8655.61	17175.48	8651.65	17168.9
70	69.8(13)	5.10	6.37	8655.53	17175.79	8649.69	17168.7
90	90.6(2)	3.80	6.94	8655.59	17175.40	8649.02	17169.2
100	100	3.64	-	8655.54	-	8648.94	-

Red: estimated errors.

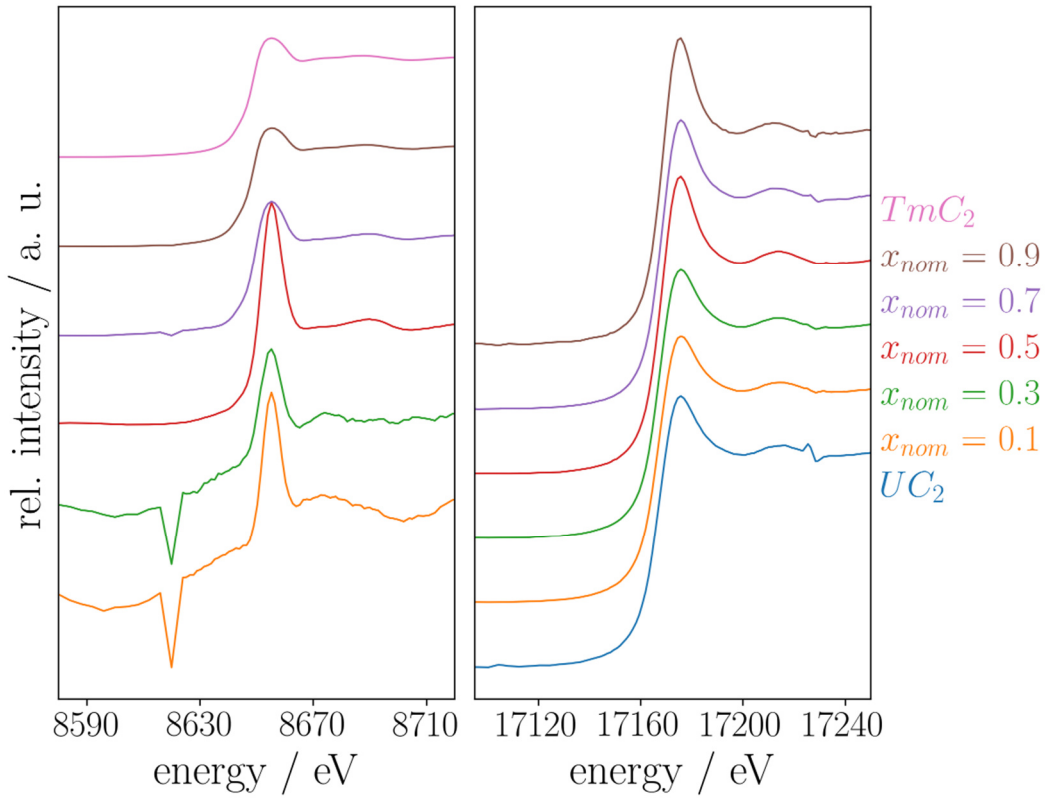

Figure S9.1. XANES spectra of $Tm_xU_{1-x}C_2$ at the Tm-L_{III} (left) and U-L_{III} edge (right).

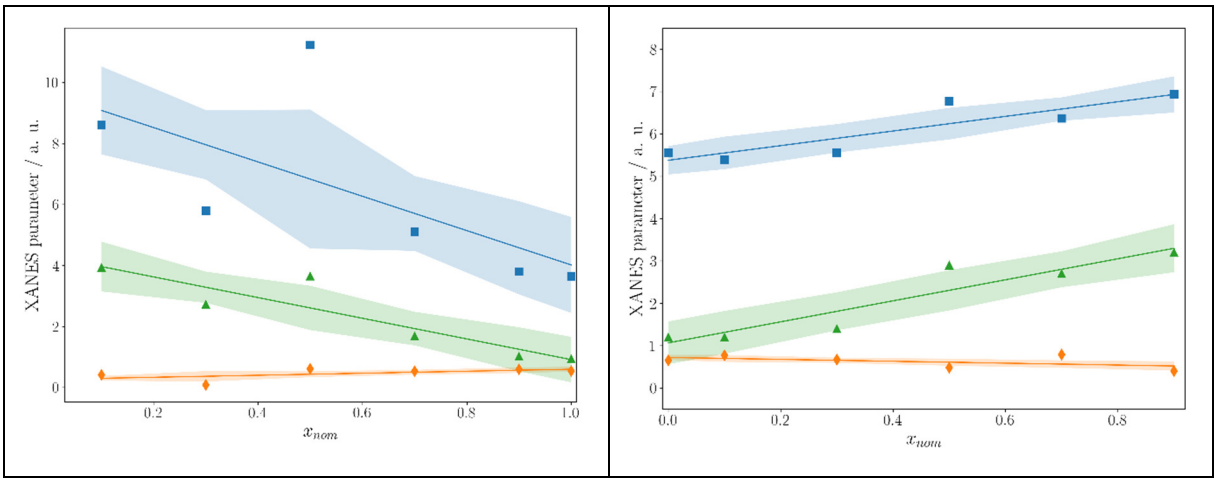

Figure S9.2. Graphical summary of the results of the XANES spectra of $Tm_xU_{1-x}C_2$ at the Tm-L_{III} (left) and U-L_{III} edge (right); blue: area of white line (A_{WL}), green: energy of white line (E_{WL}), orange: energy of absorption edge (E_0). The shaded areas correspond to confidence intervals of 68 %.

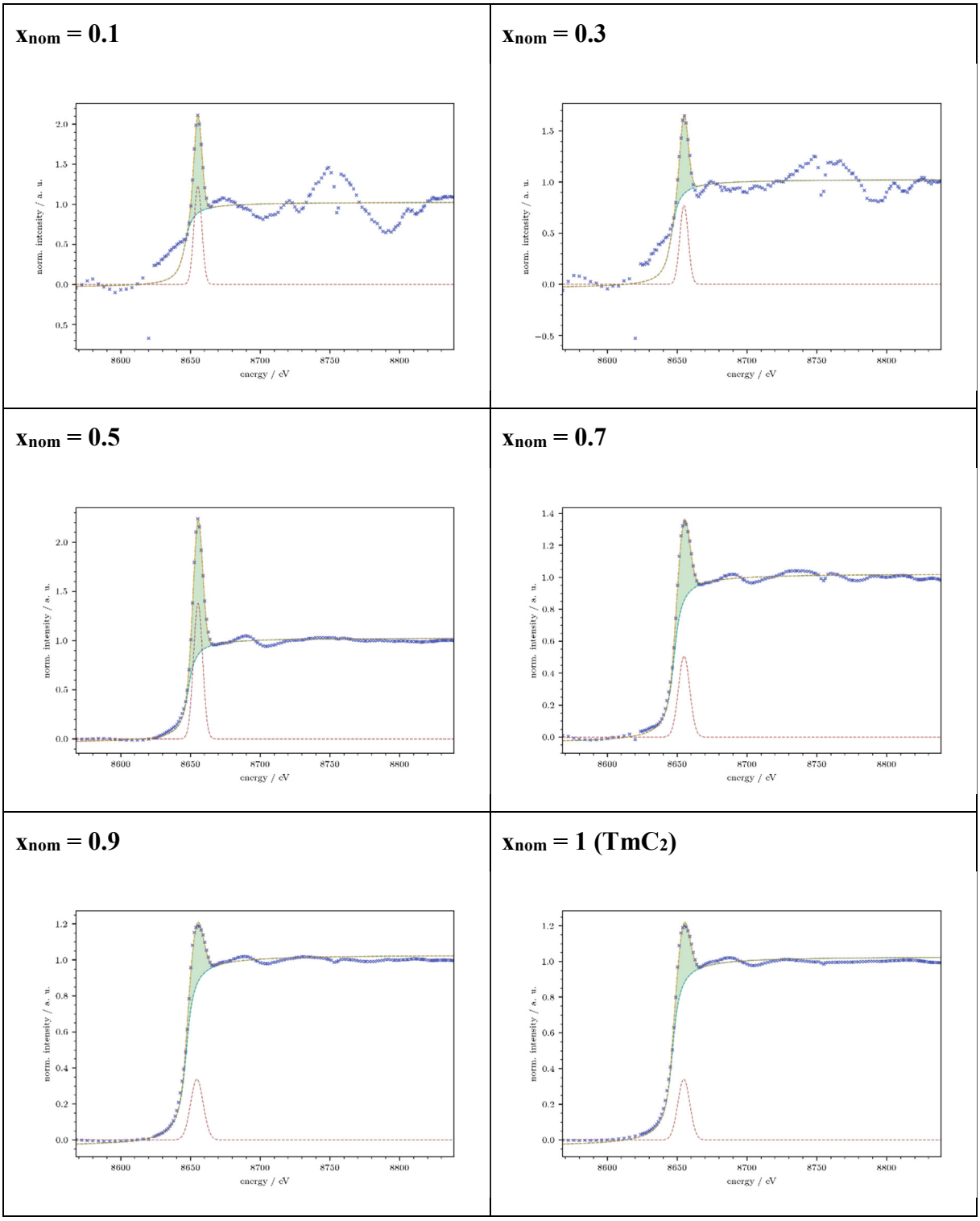

Figure S9.3. Fits of the XANES spectra of $Tm_xU_{1-x}C_2$ at the Tm-L_{III} edge.

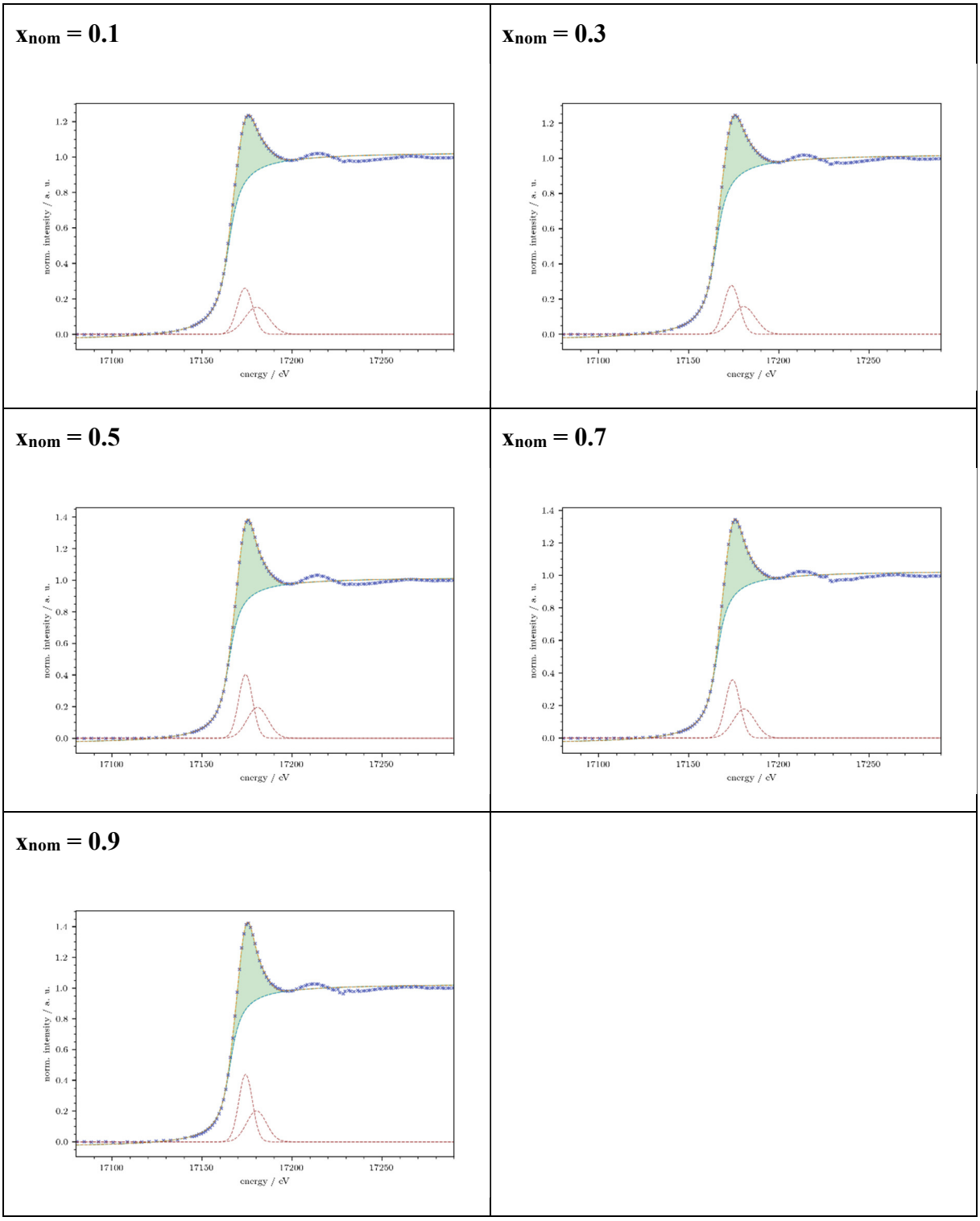

Figure S9.4. Fits of the XANES spectra of $Tm_xU_{1-x}C_2$ at the U-L_{III} edge; x = 0 (UC_2) see Figure S6.4.

Table S10. Summary of results of XANES spectra of $Lu_xU_{1-x}C_2$.

x_{nom} / %	A_{WL} / a.u.		E_{WL} / eV		E_0 / eV	
	Lu-L_{III}	U-L_{III}	Lu-L_{III}	U-L_{III}	Lu-L_{III}	U-L_{III}
0	-	5.56	-	17175.65	-	17167.2
12.5	9.06	5.61	9252.96	17175.94	9249.27	17168.2
25	7.82	5.21	9252.94	17175.86	9248.78	17167.0
50	6.24	5.83	9252.86	17175.69	9247.86	17167.8
75	5.00	6.77	9252.88	17175.62	9247.40	17168.9
87.5	2.63	7.42	9253.00	17175.48	9245.69	17168.8
100 (Lu_4C_7)	4.10	-	9252.87	-	9245.40	-

Red: estimated errors.

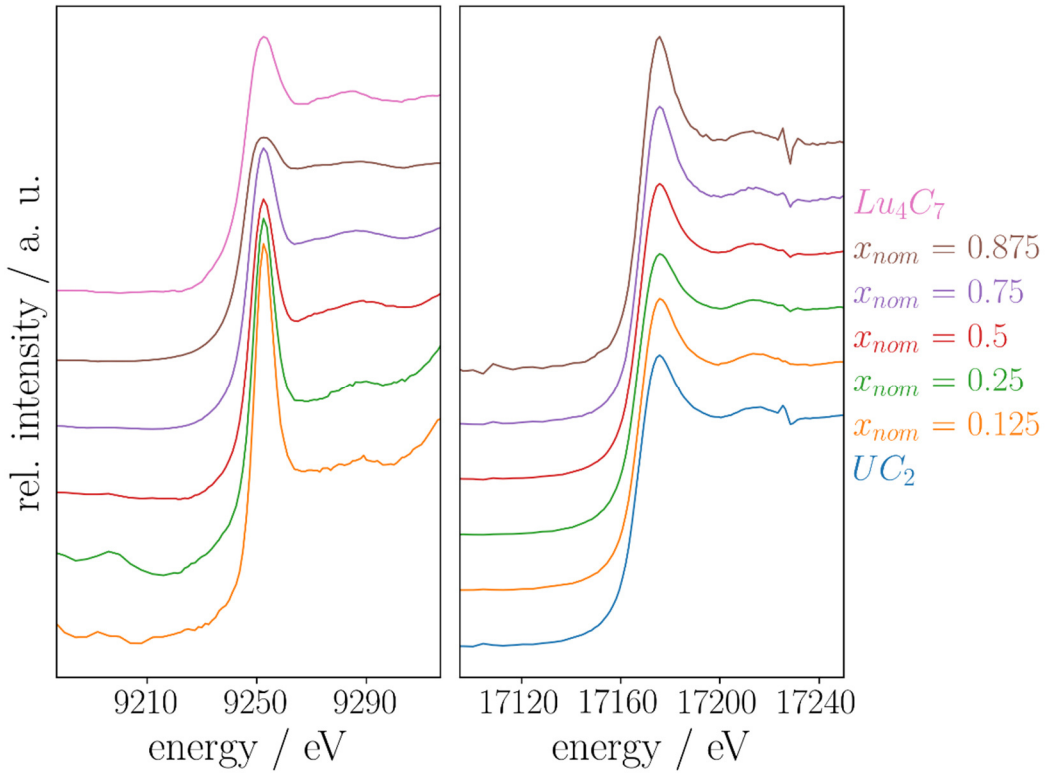

Figure S10.1. XANES spectra of $Lu_xU_{1-x}C_2$ at the Lu-L_{III} (left) and U-L_{III} edge (right).

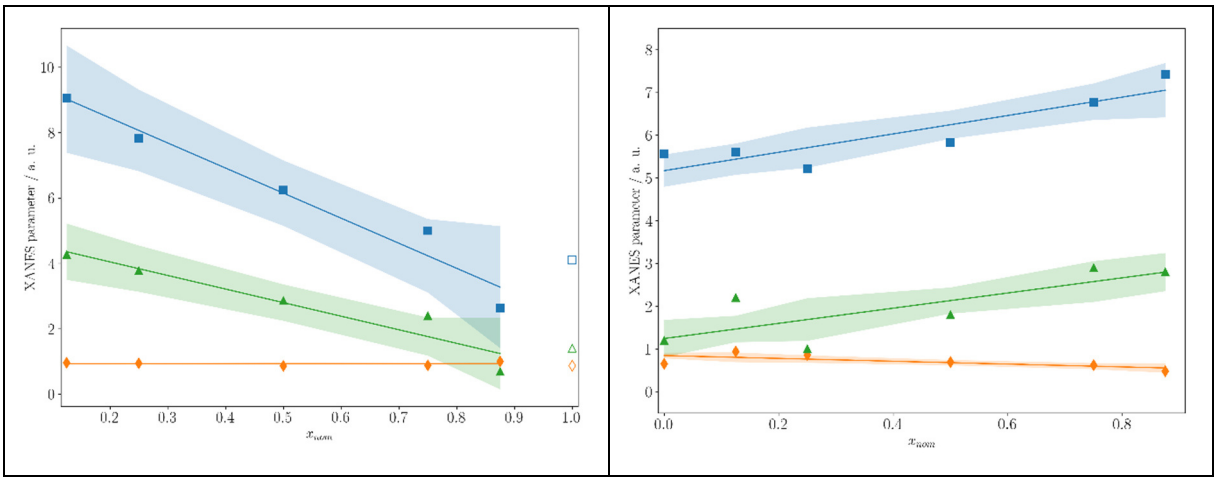

Figure S10.2. Graphical summary of the results of the XANES spectra of $Lu_xU_{1-x}C_2$ at the Lu-L_{III} (left) and U-L_{III} edge (right); blue: area of white line (A_{WL}), green: energy of white line (E_{WL}), orange: energy of absorption edge (E_0). The shaded areas correspond to confidence intervals of 68 %.

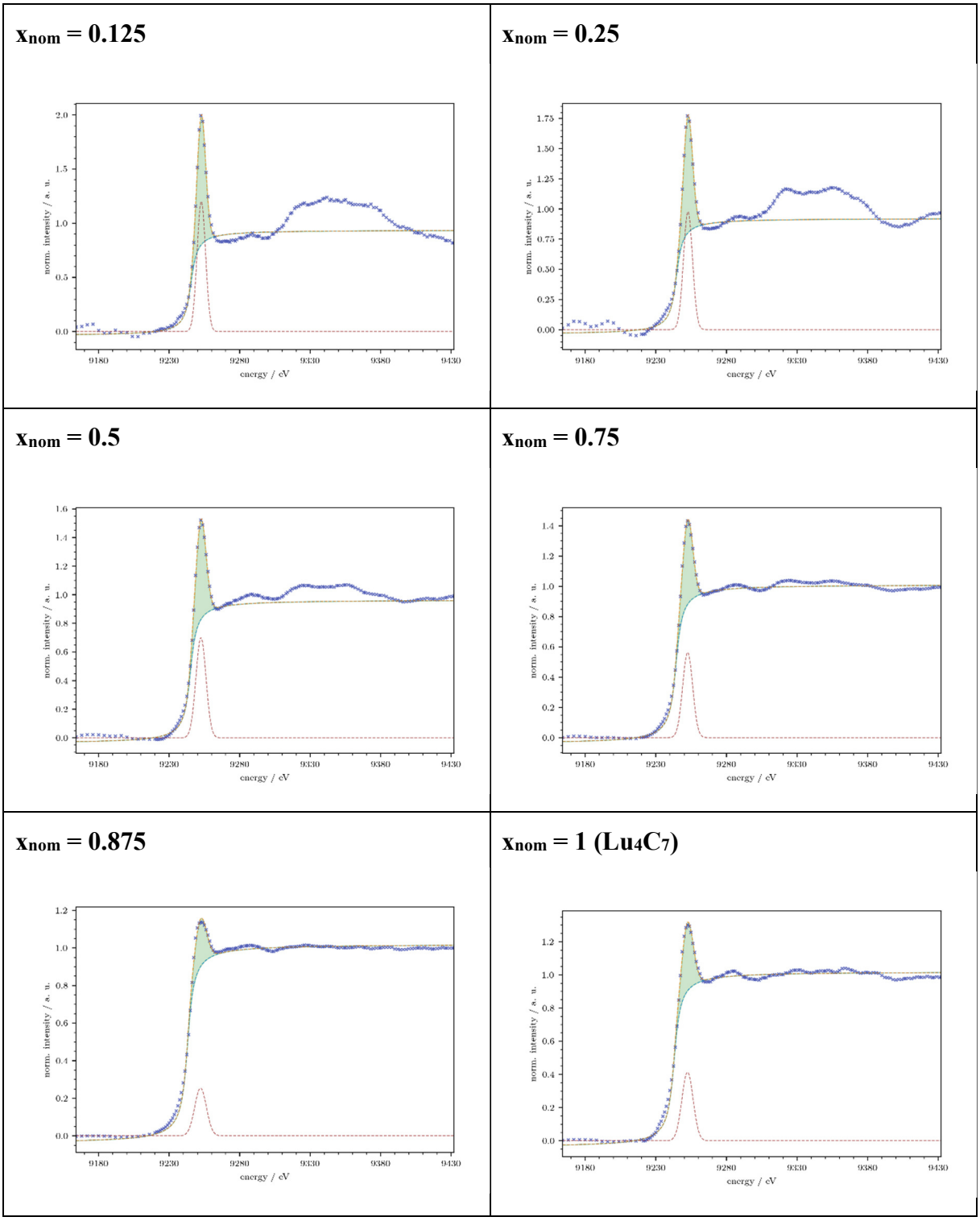

Figure S10.3. Fits of the XANES spectra of $Lu_xU_{1-x}C_2$ at the Lu-L_{III} edge.

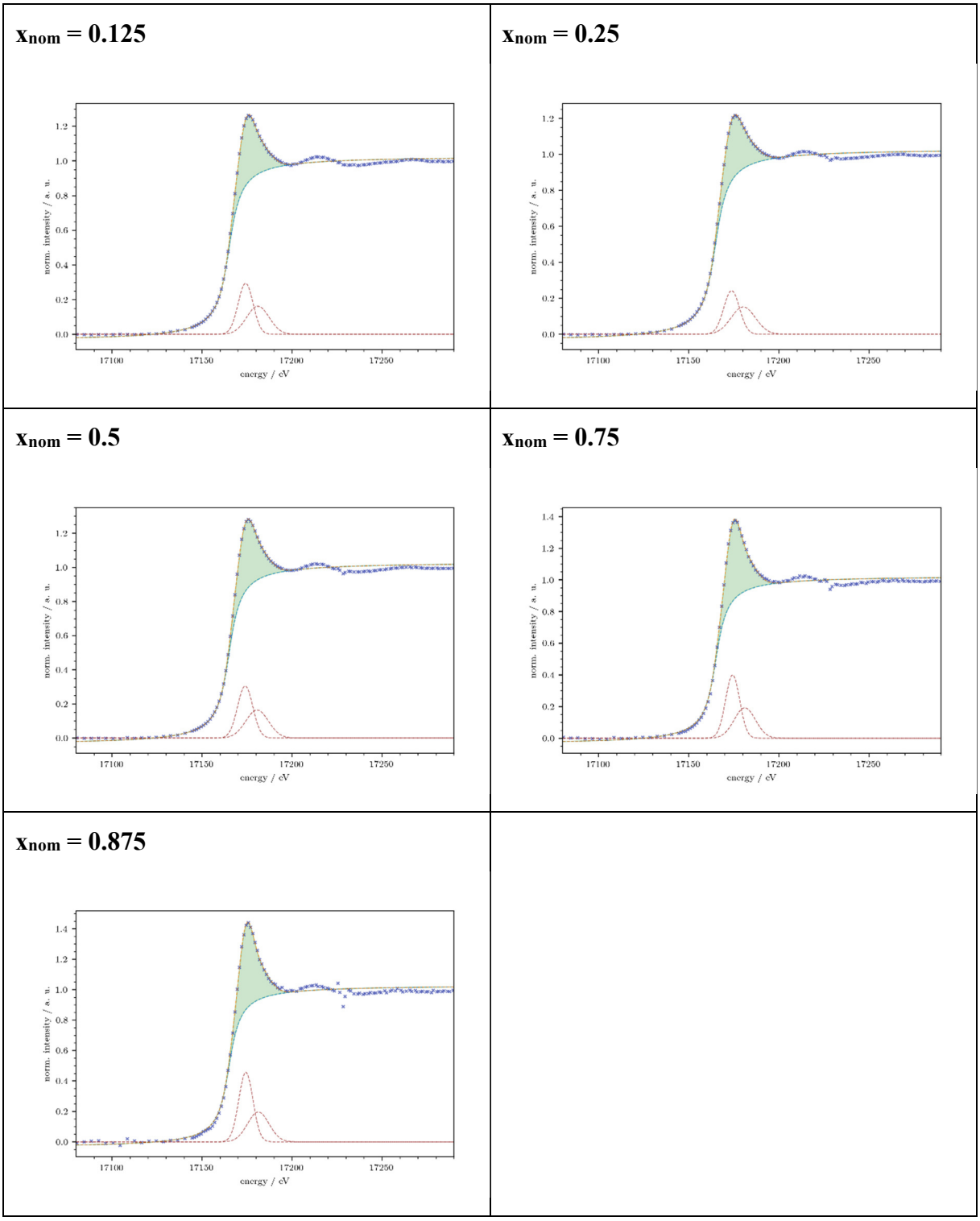

Figure S10.4. Fits of the XANES spectra of $Lu_xU_{1-x}C_2$ at the U-L_{III} edge; x = 0 (UC_2) see Figure S6.4.